Available online at www.sciencedirect.com
ScienceDirect
International Journal of Heat and Mass Transfer 51 (2008) 327–343
International Journal of HEAT and MASS TRANSFER
www.elsevier.com/locate/ijhmt

Unsteady natural convection boundary-layer flow of a linearly-stratified fluid with $Pr < 1$ on an evenly heated semi-infinite vertical plate

Wenxian Lin [a,c,*], S.W. Armfield [b], J.C. Patterson [a]

[a] School of Engineering, James Cook University, Townsville, QLD 4811, Australia
[b] School of Aerospace, Mechanical and Mechatronic Engineering, The University of Sydney, NSW 2006, Australia
[c] Solar Energy Research Institute, Yunnan Normal University, Kunming, Yunnan 650092, PR China

Received 13 October 2006; received in revised form 30 March 2007
Available online 8 June 2007

Abstract

The transient natural convection boundary-layer flow adjacent to a vertical plate heated with a uniform flux in an initially linearly-stratified ambient fluid with Prandtl number (Pr) smaller than one is investigated by scaling analysis and direct numerical simulation. The dominant parameters characterizing the flow behavior are the plate temperature, maximum vertical velocity, thermal boundary-layer thickness, whole and inner velocity boundary-layer thicknesses, and the corresponding time scales featuring these stages. Scaling laws relating these parameters to the flow governing parameters, that is Prandtl number and the dimensionless temperature stratification parameter have been obtained and validated against an exact solution and against a series of direct numerical simulations. It is shown that the scaling laws provide a good description of the flow behavior for start-up, transition and fully developed steady state. Both the scaling and numerical simulations show that the boundary layer is one dimensional away from the plate origin during start-up and at steady state, and two dimensional near the plate origin.

Keywords: Natural convection boundary layer; Scaling; Stratified flow

1. Introduction

The natural convection boundary-layer flow generated in a fluid adjacent to a heated, vertical semi-infinite plate is one of the fundamental flows in heat and mass transfer [1–5]. Most studies have examined the fully developed flow with relatively few investigations of the transient response to impulsive heating. In this study the transient response of a stably stratified fluid adjacent to a vertical semi-infinite plate subjected to an impulsively applied constant heat flux boundary condition will be investigated for low Prandtl number ($Pr < 1$). Flows with $Pr < 1$ have many important applications; in particular liquid metals with $Pr \ll 1$ have been used for rapid cooling in nuclear reactors [6–8].

Semi-analytic solutions for the steady flow adjacent to a constant heat flux vertical semi-infinite plate have been obtained by a number of workers by reducing the governing equations to a set of ordinary differential equations which are then integrated numerically [9,10]. Such an approach can be used to obtain the solution at specified Prandtl number, but does not provide scalings, and has also been shown to have difficulty dealing with very small Prandtl numbers [10]. Additional investigations of the steady flow have been carried out using the integral method of Kármán–Pohlhausen (see, e.g. [11,2]) and using singular perturbation techniques [10,12–17]. These results did not provide explicit Prandtl number scalings.

* Corresponding author. Address: School of Engineering, James Cook University, Townsville, QLD 4811, Australia. Tel.: +61 7 4781 5091; fax: +61 7 4781 6788.
E-mail address: wenxian.lin@jcu.edu.au (W. Lin).

0017-9310/$ - see front matter © 2007 Elsevier Ltd. All rights reserved.
doi:10.1016/j.ijheatmasstransfer.2007.03.040

Nomenclature

g	acceleration due to gravity
h_e	height of extra domain region
h_p	height of computational domain
l_w	length of extra domain region
L	characteristic length
N	Brunt-Väisälä frequency
p	$P/(\rho V_0^2)$
P	Pressure
Pr	Prandtl number, v/κ
Re	Reynolds number, $V_0 L/v$
s	temperature stratification parameter, $\overline{T}_Y/T_X^0$
t	time
t_p	oscillation period
t_s	time scale attaining steady state
T	temperature
$\overline{T}$	perturbation temperature
$\overline{T}_y$	ambient temperature gradient
T_w	plate temperature
T_X^0	temperature gradient across plate
u, v	U/V_0, V/V_0
U	horizontal velocity
v_m	V_m/V_0
V	vertical velocity
V_m	maximum vertical velocity
V_0	characteristic velocity
x, y	X/L, Y/L
X	horizontal coordinate
Y	vertical coordinate

Greek symbols

β	thermal expansion coefficient
δ_T, δ_v, δ_{vi}	Δ_T/L, Δ_v/L, Δ_{vi}/L
κ	thermal diffusivity
v	kinematic viscosity
θ	$T/(T_X^0 L)$
ρ	fluid density
τ, τ_p, τ^s	$t/(L/V_0)$, $t_p/(L/V_0)$, $t_s/(L/V_0)$
ΔT	$T_X^0 \Delta_T$
Δ_T	thermal boundary-layer thickness
Δ_v	outer velocity boundary-layer thickness
Δ_{vi}	inner velocity boundary-layer

Subscripts

t, X, Y	first partial derivative with respect to t, X, Y
τ, x, y	first partial derivative with respect to τ, x, y
xx, yy	second partial derivative with respect to xx, yy
XX, YY	second partial derivative with respect to XX, YY
,e	at the end of start-up stage
,p	half-period of oscillation
,s	at steady state

Park and Carey [13] combined a matched asymptotic expansion technique with an explicit finite-difference scheme to investigate the transient natural convection flow near a vertical surface at low Prandtl number; Sammouda, Belghith and Surry [8] used a finite element simulation to investigate the transient natural convection of low Prandtl number fluids in a heated cavity; The low Prandtl number natural convection in volumetrically heated rectangular enclosures with different aspect ratios was explored by direct numerical two-dimensional simulation by Piazza, Ciofalo and Arcidiacono [18–20].

The investigations cited above focused on the unsteady natural convection boundary-layer flow in an initially quiescent homogeneous ambient fluid. However, in many problems of practical interest the ambient fluid is at a non-uniform temperature, and is typically stably stratified. Park and Hyun [21,22] investigated the transient adjustment process of an initially stationary and stably stratified fluid in a square container with highly conducting boundary walls, while Chamkha [23] investigated the laminar hydromagnetic natural convection flow along a heated vertical surface in a stratified environment with internal heat absorption. Shapiro and Fedorovich [24] obtained the exact solution for the start-up and transition to steady state for the natural convection flow adjacent to an infinite vertical plate with stratified ambient using a Laplace transform technique that could only be applied at $Pr = 1$. In a later paper [25] they used a regular perturbation expansion to extend the solution to Prandtl numbers near $Pr = 1$ and obtained numerical solutions for $Pr = 0.71$ and 7.1. The natural convection boundary-layer flow of an initially linearly-stratified Newtonian fluid adjacent to an infinite vertical plate heated with a uniform flux at steady state has an exact one-dimensional solution [26] which will be detailed in Section 2.5. This steady-state flow behavior was investigated by Bejan [4] using a scaling analysis to obtain scaling laws for the dominant parameters characterizing the steady-state flow behavior and it was found that these scaling laws are in agreement with the exact solution.

It is therefore clear that the natural convection flow adjacent to a heated vertical plate has received considerable attention. However there has been no study that examines the Prandtl number effect on the flow behavior adjacent to an evenly heated semi-infinite plate with a stratified ambient for low Prandtl numbers for the complete problem of start-up, transition and full development, which motivates the present investigation.

In this study, we will develop various scaling laws for the dominant parameters characterizing the transient behavior of an unsteady natural convection boundary-layer flow of an initially linearly-stratified Newtonian fluid with $Pr < 1$ adjacent to a semi-infinite vertical plate heated with a

uniform flux, using the techniques detailed by Patterson and Imberger [27] and Bejan [4]. A series of direct numerical simulation (DNS) with selected values of Pr and stratification parameter s in the ranges $0.01 \leqslant Pr \leqslant 0.5$ and $0.2 \leqslant s \leqslant 5$ will be carried out to verify and quantify the scaling laws, where s is a dimensionless temperature stratification parameter representing the relative magnitude of the background stratification with respect to the temperature gradient across the plate. The exact solution given in [26] for the steady-state one-dimensional flow behavior will also be used to benchmark our DNS results and to validate those scaling laws obtained from the scaling analysis in this specific flow regime. This approach will be similar to that employed by Lin and Armfield [28–31] in an investigation of the transient cooling of an initially homogeneous fluid with $Pr \geqslant 1$ by natural convection in a vertical circular cylinder and in a rectangular container, and by Lin et al. [32] for an investigation of a vertical isothermal semi-infinite plate in a linearly-stratified fluid with $Pr > 1$.

The remainder of this paper is organized as follows. The scaling analysis and the exact solution of Prandtl [26] are presented in Section 2. The numerical methods and the DNS results benchmarked against the exact solution are described in Section 3. The scaling laws are then validated and quantified in Section 4 by a series of DNS results with selected values of Pr and s mentioned above. Finally, conclusions are presented in Section 5.

2. Scaling analysis

Under consideration is the unsteady natural convection boundary-layer flow of a linearly-stratified Newtonian fluid with $Pr < 1$ adjacent to a semi-infinite vertical plate heated with a uniform heat flux (see Fig. 1). The fluid is assumed to be two-dimensional and is initially at rest. The background stratification and the uniform heat flux imposed on the plate are quantified respectively by the vertical temperature gradient $\overline{T}_Y$ and the temperature gradient across the plate T^0_X. Both $\overline{T}_Y$ and T^0_X are assumed to be constants.

The governing equations of motion are the Navier–Stokes equations expressed in two-dimensional incompressible form with the Boussinesq approximation for buoyancy, which together with the temperature transport equation are as follows,

$$U_t + UU_X + VU_Y = -\frac{1}{\rho}P_X + \nu(U_{XX} + U_{YY}) \tag{1}$$

$$V_t + UV_X + VV_Y = -\frac{1}{\rho}P_Y + \nu(V_{XX} + V_{YY}) + g\beta T \tag{2}$$

$$U_X + V_Y = 0, \tag{3}$$

$$T_t + UT_X + VT_Y + V\overline{T}_Y = \kappa(T_{XX} + T_{YY}) \tag{4}$$

where U and V are the velocity components in the X and Y directions, t is the time, P is the pressure, β, κ and ν are the coefficient of thermal expansion, thermal diffusivity and kinematic viscosity of the fluid respectively, and g is the acceleration due to gravity. The temperatures in the equations are represented as the sum of the ambient temperature $\overline{T}$ and a perturbation T from the ambient temperature. The parameters which control the flow are Pr and s, where $Pr = \nu/\kappa$ and $s = \overline{T}_Y/T^0_X$ is the dimensionless temperature stratification parameter representing the relative extent of the background stratification with respect to the temperature gradient across the plate, as mentioned above. The initial and boundary conditions will be presented in Section 3.1.

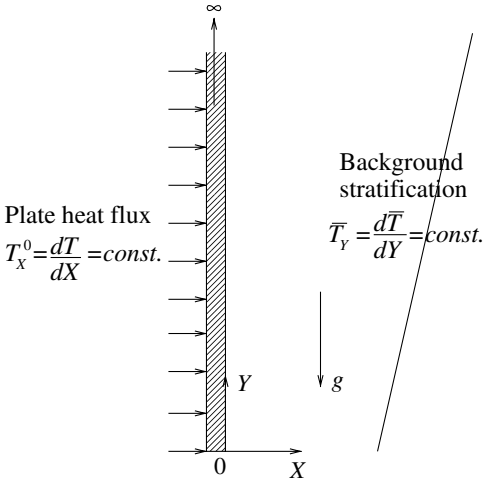

Fig. 1. Schematic depiction of the physical system considered.

Fig. 2 presents the DNS results of typical time series of several dominant parameters characterizing the behavior of the flow considered for the specific case of $Pr = 0.1$ and $s = 1$. The parameters shown are the non-dimensional plate temperature, maximum vertical velocity, thermal boundary-layer thickness, and whole and inner velocity boundary-layer thicknesses as well as the time scales representing the flow development at different stages. From these DNS results, it is seen that after the initiation of the flow (at $t = 0$), heat will be transferred via pure conduction to a thin fluid layer adjacent to the plate and a vertical thermal boundary layer forms. As the fluid within the layer has a higher temperature than the local background fluid, the fluid will move upwards under the influence of buoyancy, resulting in a velocity boundary layer which develops within the thermal boundary layer. After a short start-up development stage, both boundary layers will undergo a lengthy transitional stage, at which gradually decaying oscillations dominate the flow development, as shown in Fig. 2. When all the oscillations eventually die down, the boundary layers attain a steady state.

The oscillations presented at the transitional stage are the intrinsic properties of flows in stratified fluids, as pointed out by Turner [33]. For brevity and clarification, the parameters and the corresponding times at the end of the start-up stage and at steady state are denoted with the symbols "$,e$" and "$,s$" respectively in the subscripts whereas the corresponding half-periods of the oscillations presented in the profiles of these parameter are denoted

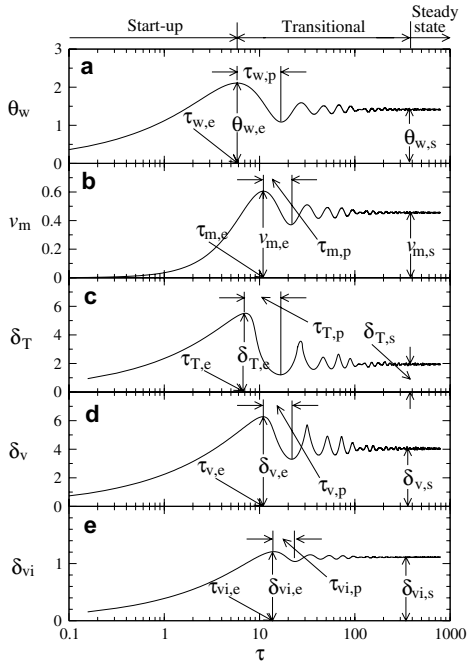

Fig. 2. Typical time series of (a) plate temperature θ_w; (b) maximum vertical velocity v_m; (c) thermal boundary-layer thickness δ_T; (d) whole velocity boundary-layer thickness δ_v; and (e) inner velocity boundary-layer thickness δ_{vi}, respectively, at height $y = 90$ for the specific case of $Pr = 0.1$ and $s = 1$. All temperatures, velocities, lengths and times were made dimensionless by $T_X^0 L$, V_0, L and L/V_0, respectively, where L and V_0 are the steady-state thermal boundary-layer thickness scale and vertical velocity scale which will be defined in Section 2.4.

with the symbol "$,p$" in the subscripts, as depicted in Fig. 2. Scaling laws at different stages of flow development will be developed in the following scaling analysis for these dominant parameters which characterize the flow behavior.

2.1. At the start-up stage

The start-up stage is initially dominated by the heat transfer via conduction through the plate, resulting in a vertical thermal boundary layer of thickness $O(\Delta_T)$ adjacent to the plate. Within the boundary layer, from Eq. (4), the dominant balance for $Pr < 1$ is that between the unsteady term $O(\Delta T/t)$ and the conduction normal to the wall $O(\kappa \Delta T/\Delta_T^2)$, where $\Delta T = T_X^0 \Delta_T$ is the total temperature variation over the boundary layer, giving,

$$\Delta_T \sim \kappa^{1/2} t^{1/2}. \tag{5}$$

The plate temperature T_w is then

$$T_w \sim T_X^0 \Delta_T \sim T_X^0 \kappa^{1/2} t^{1/2}. \tag{6}$$

At the same time, a velocity boundary layer forms within the thermal boundary layer due to the buoyancy, as discussed above. It consists of an inner region and an outer region, with the location at which the maximum vertical velocity V_m is attained as the appropriate dividing point. The width of this dividing location is then the inner velocity boundary-layer thickness Δ_{vi}. Within Δ_{vi} (near the plate), the dominant balance in Eq. (2) is between the unsteady term $O(V_m/t)$ and the viscosity $O(\nu V_m/\Delta_{vi}^2)$, which gives,

$$\Delta_{vi} \sim \nu^{1/2} t^{1/2} \sim Pr^{1/2} \Delta_T. \tag{7}$$

For $Pr < 1$, Δ_{vi} will be always smaller than Δ_T, meaning that the inner velocity boundary layer is embedded within the thermal boundary layer. Away from the plate, the viscosity over the thermal boundary layer is $O(\nu V_m/\Delta_T^2)$ and

$$\frac{\text{Unsteady term}}{\text{Viscosity over } \Delta_T} \sim \frac{V_m/t}{\nu V_m/(\kappa t)} \sim \frac{1}{Pr} > 1, \tag{8}$$

that is, in the outer region the dominant balance is between the unsteady term and buoyancy. So buoyancy acts to accelerate the fluid only over the outer region $(\Delta_T - \Delta_{vi})$, which is

$$\Delta_T - \Delta_{vi} \sim \kappa^{1/2} t^{1/2} - \nu^{1/2} t^{1/2} \sim \kappa^{1/2}(1 - Pr^{1/2}) t^{1/2}. \tag{9}$$

Therefore the appropriate buoyancy term to be used in the balance between the unsteady and buoyancy terms in Eq. (2) is $g\beta T_X^0 \kappa^{1/2}(1 - Pr^{1/2}) t^{1/2}$, giving,

$$\frac{V_m}{t} \sim g\beta T_X^0 \kappa^{1/2}(1 - Pr^{1/2}) t^{1/2}, \tag{10}$$

that is,

$$V_m \sim g\beta T_X^0 \kappa^{1/2}(1 - Pr^{1/2}) t^{3/2}. \tag{11}$$

This continues until there is a balance between the convection of heat carried away by the boundary-layer flow $O(V_m \Delta T/Y + V_m \overline{T}_Y)$ and the conduction of heat transferred in across the boundary, that is, when

$$V_m \left(\frac{T_X^0 \Delta_T}{Y} + s T_X^0 \right) \sim \frac{\kappa T_X^0 \Delta_T}{\Delta_T^2}, \tag{12}$$

At this time the development of the thermal boundary layer comes to the end of the start-up stage.

The first of the advection terms is the same as that in the non-stratified case [34], while the second is that associated with the background stratification. If the former is dominant then the boundary layer at the end of the start-up stage will behave the same as that for the non-stratified case [34] and $\Delta_T \sim Y^{1/5}$, in which case this term may be written as

$$\frac{T_X^0 \Delta_T}{Y} \sim \frac{T_X^0}{Y^{4/5}}, \tag{13}$$

which reduces with increasing Y. This term will therefore be dominant for small enough Y at which the boundary layer will behave identically to the non-stratified case. On the other hand, if the ratio of $T_X^0 \Delta_T/Y$ and $s T_X^0$ is small enough, the second term dominates, as

$$\frac{T_X^0 \Delta_T}{Y} / (s T_X^0) \sim \frac{T_X^0 \kappa^{1/2} t^{1/2}}{Y s T_X^0} \sim \frac{\kappa^{1/2} t^{1/2}}{Ys} < 1, \tag{14}$$

for large enough Y and s and small enough t. Thus for $T_X^0 \Delta_T/Y \ll s T_X^0$, the appropriate balance is obtained from the second of the advection terms as

$$sV_m \sim \frac{\kappa}{\Delta_T} \sim \frac{\kappa^{1/2}}{t^{1/2}}. \tag{15}$$

In this paper, we will focus our study on this $T_X^0 \Delta_T / Y \ll sT_X^0$ case.

Matching the two V_m's in Eqs. (11) and (15) gives

$$g\beta T_X^0 \kappa^{1/2}(1 - Pr^{1/2})t^{3/2} \sim \frac{\kappa^{1/2}}{st^{1/2}}, \tag{16}$$

which leads to

$$t_{T,e} \sim \frac{1}{s^{1/2}(g\beta T_X^0)^{1/2}(1 - Pr^{1/2})^{1/2}}. \tag{17}$$

$t_{T,e}$ represents the time for the development of the thermal boundary layer to come to the end of the start-up stage.

At this time, the thermal boundary-layer thickness $\Delta_{T,e}$, from Eq. (5), is

$$\Delta_{T,e} \sim \frac{\kappa^{1/2}}{s^{1/4}(g\beta T_X^0)^{1/4}(1 - Pr^{1/2})^{1/4}}, \tag{18}$$

and the maximum vertical velocity $V_{T,e}$, from Eq. (11), is

$$V_{T,e} \sim \frac{\kappa^{1/2}(g\beta T_X^0)^{1/4}(1 - Pr^{1/2})^{1/4}}{s^{3/4}}, \tag{19}$$

the plate temperature $T_{T,e}$ is then obtained from $\Delta_{T,e}$ as

$$T_{T,e} \sim T_X^0 \Delta_{T,e} \sim \frac{T_X^0 \kappa^{1/2}}{s^{1/4}(g\beta T_X^0)^{1/4}(1 - Pr^{1/2})^{1/4}}, \tag{20}$$

and the inner velocity boundary-layer thickness $\Delta_{vi,T,e}$, from Eq. (7), is

$$\Delta_{vi,T,e} \sim \frac{\nu^{1/2}}{s^{1/4}(g\beta T_X^0)^{1/4}(1 - Pr^{1/2})^{1/4}} \sim Pr^{1/2}\Delta_{T,e}. \tag{21}$$

During the start-up stage, as illustrated in Fig. 2, the whole (inner plus outer) velocity boundary layer for $Pr < 1$ will be as wide as the thermal boundary layer due to the presence of buoyancy, and it is therefore expected that the whole velocity boundary-layer thickness $\Delta_{v,T,e}$ at $t = t_{T,e}$ will have the same scale as $\Delta_{T,e}$ and the scaling law (18) will also be applicable to $\Delta_{v,T,e}$.

It should be noted that for $Pr < 1$, when the development of the thermal boundary layer attains the end of its start-up stage (that is when $t = t_{T,e}$), the development of the velocity boundary layer (both inner and whole) and the maximum vertical velocity have not yet attained the ends of their respective start-up states, that is, $t_{vi,e} > t_{T,e}$, $\Delta_{vi,e} > \Delta_{vi,T,e}$, $t_{v,e} > t_{T,e}$, $\Delta_{v,e} > \Delta_{v,T,e}$, $t_{m,e} > t_{T,e}$, and $V_{m,e} > V_{T,e}$, as will be shown in Section 4.

If we use $\Delta_{vi,T,e}$ for the viscosity term and $(\Delta_{T,e} - \Delta_{vi,T,e})$ for the buoyancy term, then the ratio of viscosity and the buoyancy at this time is

$$\nu \frac{V_{T,e}}{\Delta_{vi,T,e}^2} / [g\beta T_X^0(\Delta_{T,e} - \Delta_{vi,T,e})] \sim \frac{\nu V_{T,e}}{Pr\Delta_{T,e}^2 g\beta T_X^0 \Delta_{T,e}(1 - Pr^{1/2})} \sim 1. \tag{22}$$

This is just a reflection of the fact that at this time the viscosity balances the unsteady term in the inner region and therefore also balances the buoyancy over the outer boundary layer.

However, the viscosity calculated over the whole layer (inner and outer regions) must ultimately balance the buoyancy for steady state to be achieved. At this stage, the ratio of the two terms is

$$\nu \frac{V_{T,e}}{\Delta_{T,e}^2} / [g\beta T_X^0 \Delta_{T,e}] \sim \frac{\nu V_{T,e}}{\Delta_{T,e}^3 g\beta T_X^0} \sim Pr(1 - Pr^{1/2}) < 1 \tag{23}$$

for $Pr < 1$, which demonstrates that at this time no balance exists between the viscosity and buoyancy.

An examination of the scaling laws (5), (6), (7), and (11) obtained above reveals that the flow development until the end of the start-up stage of the thermal boundary layer is one-dimensional and independent of Y. However, at the end of the start-up stage, this one-dimensional structure will be true only for $T_X^0 \Delta_T / Y \ll sT_X^0$, as noted above. With Eq. (18), this implies that the condition

$$Y \gg \frac{\kappa^{1/2}}{s^{5/4}(g\beta T_X^0)^{1/4}(1 - Pr^{1/2})^{1/4}}, \tag{24}$$

has to be met. If $Y \lesssim Y_{c,e}$, where $Y_{c,e} = \kappa^{1/2} s^{-5/4} \times (g\beta T_X^0)^{-1/4}(1 - Pr^{1/2})^{-1/4}$, the flow development will behave the same as that in the non-stratified case [34] which is two-dimensional and Y dependent, as sketched in Fig. 3. Therefore, $Y_{c,e}$ represents the change-over height at which the one-dimensional flow development becomes two-dimensional. Hence, the scaling laws (17)–(21) are only valid for $Y \gg Y_{c,e}$.

2.2. At steady state

After $t > t_{T,e}$, the conduction–convection balance dominates in Eq. (4), which gives,

$$V_m s T_X^0 \sim \kappa \frac{\Delta T}{\Delta_T^2} \sim \kappa \frac{T_X^0 \Delta_T}{\Delta_T^2} \sim \kappa \frac{T_X^0}{\Delta_T}, \tag{25}$$

that is,

$$\Delta_T \sim \frac{\kappa}{sV_m}. \tag{26}$$

It should be noted that Δ_T is no longer governed by $\kappa^{1/2}t^{1/2}$ for $t > t_{T,e}$, but Δ_v is still governed by $\nu^{1/2}t^{1/2}$.

It is now also necessary to consider the buoyancy term over the whole layer, that is,

$$V_m \sim g\beta T_X^0 \Delta_T t, \tag{27}$$

which holds until the flow attains steady state. At steady state, $\Delta_T \sim \Delta_v \sim \nu^{1/2}t^{1/2}$, which, together with Eq. (26), gives the time scale t_s to attain steady state,

$$t_s \sim \frac{1}{s^{1/2}Pr^{1/2}(g\beta T_X^0)^{1/2}}. \tag{28}$$

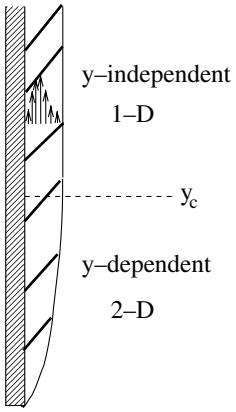

Fig. 3. Boundary layer structures: one-dimensional when $y \gg y_c$ and two-dimensional when y smaller than y_c, where $y_c = y_{c,e}$ and $y_{c,s}$ are for the end of start-up stage and for the steady state respectively.

Hence at steady state, that is when $t > t_s$, the thermal boundary-layer thickness becomes

$$\Delta_{T,s} \sim v^{1/2} t_s^{1/2} \sim \frac{v^{1/2}}{s^{1/4} Pr^{1/4} (g\beta T_X^0)^{1/4}}, \tag{29}$$

which is also valid for both the steady-state inner and whole velocity boundary-layer thicknesses $\Delta_{vi,s}$ and $\Delta_{v,s}$, the plate temperature $T_{w,s}$ becomes

$$T_{w,s} \sim T_X^0 \Delta_{T,s} \sim \frac{T_X^0 v^{1/2}}{s^{1/4} Pr^{1/4} (g\beta T_X^0)^{1/4}}, \tag{30}$$

and the maximum velocity becomes

$$V_{m,s} \sim g\beta T_X^0 v^{1/2} t_s^{3/2} \sim \frac{(g\beta T_X^0)^{1/4} v^{1/2}}{s^{3/4} Pr^{3/4}}. \tag{31}$$

As $t_s/t_{T,e} \sim (1 - Pr^{1/2})^{1/2}/Pr^{1/2} > 1$ for $Pr < 1$, the maximum velocity V_m for $t_{T,e} < t < t_s$ is, from Eqs. (26) and (27), as follows:

$$V_m \sim \frac{(g\beta T_X^0)^{1/2} \kappa^{1/2} t^{1/2}}{s^{1/2}}. \tag{32}$$

The condition $T_X^0 \Delta_T / Y \ll s T_X^0$, with Eq. (29), implies that

$$Y \gg \frac{v^{1/2}}{s^{5/4} Pr^{1/4} (g\beta T_X^0)^{1/4}}, \tag{33}$$

therefore, all the scaling laws obtained above for the steady state, that is Eqs. (29)–(31), are only valid when $Y \gg Y_{c,s}$, where $Y_{c,s} = v^{1/2} s^{-5/4} Pr^{-1/4} (g\beta T_X^0)^{-1/4}$, similar to $Y_{c,e}$, represents the change-over height at which the steady-state one-dimensional flow development becomes two-dimensional.

2.3. At the transitional stage

For flows in a stratified fluid, oscillations will be present at the transitional stage, as observed above, which have the Brunt-Väisälä frequency N [33] given by,

$$N = \left[g\beta \frac{\partial \overline{T}(Y)}{\partial Y} \right]^{1/2} = s^{1/2} (g\beta T_X^0)^{1/2}. \tag{34}$$

Hence, the oscillations have the following period:

$$t_p = \frac{2\pi}{N} \sim \frac{1}{s^{1/2} (g\beta T_X^0)^{1/2}}. \tag{35}$$

This relation is then the scaling law for $t_{w,p}$, $t_{m,p}$, $t_{T,p}$, $t_{v,p}$, and $t_{vi,p}$.

The amplitudes of the oscillations ("overshoots") are scaled with the difference between the values of the parameters T_w, V_m, Δ_T, Δ_v, and Δ_{vi} at the end of the start-up stage and those at steady state, which are apparently Pr dependent. For example, the amplitude of the oscillation presented in the time series of the wall temperature is scaled with $(T_{w,e} - T_{w,s})$, and the scaling laws (20) and (30) show that

$$\frac{T_{w,e}}{T_{w,s}} \sim \frac{1}{Pr^{1/4} (1 - Pr^{1/2})^{1/4}}, \tag{36}$$

indicating that smaller Pr fluids will have larger "overshoots" at the transitional stage.

2.4. Non-dimensionalized scaling laws

The scaling laws obtained above can be made dimensionless by appropriate characteristic length, velocity, time and temperature scales featuring the flow. It is natural, from Eqs. (29)–(31), to choose $L = v^{1/2} s^{-1/4} Pr^{-1/4} \times (g\beta T_X^0)^{-1/4}$, $V_0 = v^{1/2} (g\beta T_X^0)^{1/4} s^{-3/4} Pr^{-3/4}$, L/V_0, and $T_X^0 L$ as the respective characteristic length, temperature, time, and velocity scales for the flow considered. With these characteristic scales, the scaling laws obtained above can be made dimensionless as follows.

During the start-up stage, the scaling laws (5), (6), (7), and (11) will have the following dimensionless forms:

$$\delta_T = \frac{\Delta_T}{L} \sim s^{1/2} \tau^{1/2}, \tag{37}$$

$$\theta_w = \frac{T_w}{T_X^0 L} \sim \delta_T \sim s^{1/2} \tau^{1/2}, \tag{38}$$

$$\delta_{vi} = \frac{\Delta_{vi}}{L} \sim Pr^{1/2} s^{1/2} \tau^{1/2}, \tag{39}$$

$$v_m = \frac{V_m}{V_0} \sim s^{3/2} Pr (1 - Pr^{1/2}) \tau^{3/2}, \tag{40}$$

where $\tau = t/(L/V_0)$ is the dimensionless time. Apparently Eq. (37) or (38) will also be applicable to the dimensionless $\delta_v = \Delta_v/L$. It should be noted, as noted above, that the scaling laws (37)–(40) are valid for $t < t_{T,e}$, or in non-dimensional term for $\tau < \tau_{T,e}$, where, from Eq. (17),

$$\tau_{T,e} = \frac{t_{T,e}}{(L/V_0)} \sim \frac{1}{s Pr^{1/2} (1 - Pr^{1/2})^{1/2}}. \tag{41}$$

At the end of the start-up stage of the thermal boundary layer development (that is at $\tau_{T,e}$), the scaling laws (18)–(21) will have the following dimensionless forms

$$\delta_{T,e} = \frac{\Delta_{T,e}}{L} \sim \frac{1}{Pr^{1/4}(1-Pr^{1/2})^{1/4}}, \tag{42}$$

$$v_{T,e} = \frac{V_{T,e}}{V_0} \sim Pr^{1/4}(1-Pr^{1/2})^{1/4}, \tag{43}$$

$$\theta_{T,e} = \frac{T_{T,e}}{T_X^0 L} \sim \frac{1}{Pr^{1/4}(1-Pr^{1/2})^{1/4}}, \tag{44}$$

$$\delta_{vi,T,e} = \frac{\Delta_{vi,T,e}}{L} \sim \frac{Pr^{1/4}}{(1-Pr^{1/2})^{1/4}}. \tag{45}$$

Again Eqs. (42) or (44) will also be applicable for the dimensionless $\delta_{v,T,e} = \Delta_{v,T,e}/L$. It is also expected that Eq. (41) will be applicable to the dimensionless form of $t_{w,e}$, $t_{m,e}$, $t_{v,e}$, and $t_{vi,e}$, that is to $\tau_{w,e} = t_{w,e}/(L/V_0)$, $\tau_{m,e} = t_{m,e}/(L/V_0)$, $\tau_{v,e} = t_{v,e}/(L/V_0)$, and $\tau_{vi,e} = t_{vi,e}/(L/V_0)$.

As t_s is generally larger than $t_{T,e}$ and $t_{m,e} > t_{T,e}$ for the $Pr < 1$ fluids considered here, as will be shown in Section 4, the dimensionless maximum velocity v_m for $t_{T,e} < t < t_{m,e}$ when $t_{m,e} \leqslant t_s$ (or in dimensionless form, for $\tau_{T,e} < \tau < \tau_{m,e}$ when $\tau_{m,e} \leqslant \tau_s$) is, from Eq. (32), as follows:

$$v_m \sim s^{1/2} Pr^{1/2} \tau^{1/2}. \tag{46}$$

When $t > t_s$, that is when $\tau > \tau_s$, the development will attain steady state, as noted above, where τ_s, from Eq. (28), is,

$$\tau_s = \frac{t_s}{(L/V_0)} \sim \frac{1}{sPr}. \tag{47}$$

At steady state, the scaling laws (29)–(31) will have the following dimensionless forms

$$\delta_{T,s} = \frac{\Delta_{T,s}}{L} \sim 1, \tag{48}$$

$$\theta_{w,s} = \frac{T_{w,s}}{T_X^0 L} \sim 1, \tag{49}$$

$$v_{m,s} = \frac{V_{m,s}}{V_0} \sim 1, \tag{50}$$

Eqs. (48) or (49) will also be applicable to the dimensionless form of $\Delta_{v,s}$ and $\Delta_{vi,s}$, that is to $\delta_{v,s} = \Delta_{v,s}/L$ and $\delta_{vi,s} = \Delta_{vi,s}/L$.

The dimensionless period τ_p for the oscillations presented at the transitional stage will have the following form:

$$\tau_p = \frac{t_p}{(L/V_0)} \sim \frac{1}{sPr^{1/2}}, \tag{51}$$

which will also be the scaling law for the dimensionless form of $t_{w,p}$, $t_{m,p}$, $t_{T,p}$, $t_{v,p}$, and $t_{vi,p}$, that is for $\tau_{w,p} = t_{w,p}/(L/V_0)$, $\tau_{m,p} = t_{m,p}/(L/V_0)$, $\tau_{T,p} = t_{T,p}/(L/V_0)$, $\tau_{v,p} = t_{v,p}/(L/V_0)$, and $\tau_{vi,p} = t_{vi,p}/(L/V_0)$.

The dimensionless change-over heights $y_{c,e}$ and $y_{c,s}$ are

$$y_{c,e} = \frac{Y_{c,e}}{L} = \frac{1}{sPr^{1/4}(1-Pr^{1/2})^{1/4}}, \tag{52}$$

$$y_{c,s} = \frac{Y_{c,s}}{L} = \frac{1}{s}. \tag{53}$$

From these scaling laws, it is seen that the boundary-layer development is one-dimensional and is independent of y if $y \gg y_{c,e}$ and $y \gg y_{c,s}$, as noted above. As stated before, our current study is focusing in this one-dimensional flow regime.

2.5. Analytical solution at steady state

The governing equations (1)–(4) can be recast in non-dimensional form as follows using V_0, L, $T_X^0 L$, L/V_0 and ρV_0^2 as the characteristic velocity, length, temperature, time and pressure scales respectively,

$$u_\tau + uu_x + vu_y = -p_x + \frac{1}{Re}(u_{xx} + u_{yy}), \tag{54}$$

$$v_\tau + uv_x + vv_y = -p_y + \frac{1}{Re}(v_{xx} + v_{yy}) + \frac{1}{Re}\theta, \tag{55}$$

$$u_x + v_y = 0, \tag{56}$$

$$\theta_\tau + u\theta_x + v\theta_y + v\frac{1}{RePr} = \frac{1}{RePr}(\theta_{xx} + \theta_{yy}), \tag{57}$$

where $Re = 1/(sPr)$ is the Reynolds number, u, v, x, y, p, τ, and θ are the dimensionless forms of U, V, X, Y, P, t, and T, respectively.

At steady state, the temperature and velocity fields is independent of y when $y \gg y_{c,s}$ and the flow considered here is in the one-dimensional regime, as shown above. The scaled Eqs. (54)–(57) will allow all y derivative terms to be dropped and the following analytical solution to be obtained [26]

$$v(x) = \sqrt{2}e^{-x/\sqrt{2}} \sin\left(-\frac{x}{\sqrt{2}}\right), \tag{58}$$

$$\theta(x) = \sqrt{2}e^{-x/\sqrt{2}} \cos\left(-\frac{x}{\sqrt{2}}\right). \tag{59}$$

From this solution, it is expected that the dominant parameters will have the following values at steady state,

$$\theta_{w,s} = \sqrt{2} = 1.414 \quad \text{at } x = 0, \tag{60}$$

$$\delta_{T,s} = \sqrt{2}\frac{\pi}{2} = 2.221 \quad \text{when } \theta = 0, \tag{61}$$

$$v_{m,s} = \sqrt{2}e^{-\pi/4} \sin\left(\frac{\pi}{4}\right) = 0.455 \quad \text{at } x = \sqrt{2}\frac{\pi}{4} = 1.111, \tag{62}$$

$$\delta_{vi,s} = \sqrt{2}\frac{\pi}{4} = 1.111 \quad \text{when } v = v_{m,s}, \tag{63}$$

$$\delta_{v,s} = \sqrt{2}\pi = 4.443 \quad \text{when } v \text{ reduces to } 0. \tag{64}$$

Nevertheless, in the subsequent DNS we will define the locations when $\theta_w = 0.05\theta_{w,s}$ and $v = 0.05v_{m,s}$ as the thermal boundary-layer thickness δ_T and the whole velocity boundary-layer thickness δ_v respectively due to the numerical consideration. It is then expected that at steady state $\delta_{T,s}$ and $\delta_{v,s}$ will have the following values,

$$\delta_{T,s} = 1.940 \quad \text{when } \theta = 0.05\theta_{w,s}, \tag{65}$$

$$\delta_{v,s} = 4.040 \quad \text{when } v = 0.05v_{m,s}. \tag{66}$$

Comparing the scaling laws (48)–(50) with the analytical scales (65), (66), (62), (60), and (63), it will be found that our steady-state scaling laws obtained from the scaling analysis are apparently in line with the analytical solution.

The analytical solution at steady state will be used in the subsequent sections to benchmark the DNS results and to validate our steady-state scaling laws obtained from the scaling analysis.

3. Numerical methods and benchmark

3.1. Initial and boundary conditions

To minimize the effect of the boundaries in the DNS, the computational domain shown in Fig. 4 is used in the simulations, where an extra region with a height of $h_e = 50$ and a width of $l_w = 200$ has been added to both the top and the bottom boundaries and the following initial and boundary conditions have been used,

$$u = v = 0, \quad \theta = 0 \quad \text{at all } x, y \text{ when } \tau < 0;$$

and

$$u = v = 0,\ \theta_x = 0 \quad \text{at } x = 0,\ -h_e \leqslant y \leqslant 0;$$
$$u = v = 0,\ \theta_x = 1 \quad \text{at } x = 0,\ 0 \leqslant y \leqslant h_p;$$
$$u_x = v_x = \theta_x = 0 \quad \text{at } x = l_w,\ -h_e \leqslant y \leqslant h_p;$$
$$u = v = 0,\ \theta_y = 0 \quad \text{at } 0 \leqslant x \leqslant l_w,\ y = -h_e;$$
$$u_y = v_y = \theta_y = 0 \quad \text{at } 0 \leqslant x \leqslant l_w,\ y = h_p \text{ when } \tau \geqslant 0.$$

3.2. Numerical algorithm

The governing equations are discretized on a non-staggered mesh using finite volumes, with standard second-order central difference schemes used for the viscous, pressure gradient and divergence terms. The QUICK third-order upwind scheme is used for the advective terms. The second-order Adams–Bashforth scheme and Crank–Nicolson scheme are used for the time integration of the advective terms and the diffusive terms, respectively. To enforce continuity, the pressure correction method is used to construct a Poisson's equation which is solved using the preconditioned GMRES method. Detailed descriptions of these schemes were given in [35] and the code has been widely used for the simulation of a range of buoyancy dominated flows, such as travelling waves in natural convection in a cavity [36] and weak fountain flows [37,38].

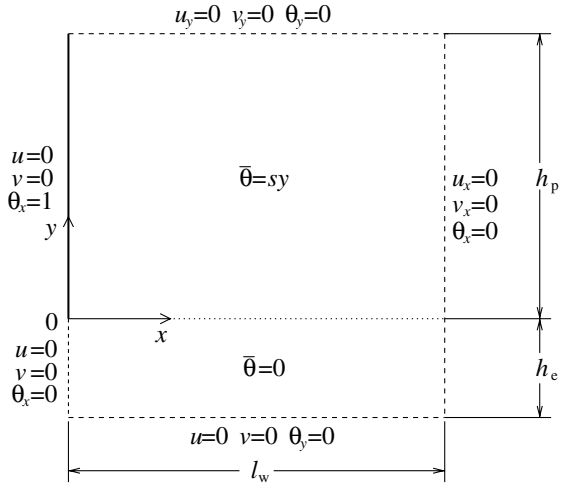

Fig. 4. Computational domain and initial and boundary conditions for the direct numerical simulations.

To ensure that a sufficiently high resolution is maintained in the numerical simulations, a non-uniform computational mesh has been used which concentrates points in the boundary layer and near the boundaries and is relatively coarse in the interior of the domain. Specifically, the mesh is constructed using a stretched grid, with nodes distributed symmetrically with respect to the half-width and half-height of the computational domain shown in Fig. 4. The nearest grid point is located 0.035 from the domain boundaries in the x-direction and 0.09 in the y-direction. Subsequently, the mesh expands at a fixed rate of 2.5% in the x-direction and 1.2% in the y-direction up to $x = y = 10$. After that, the mesh size expansion rate decreases at a rate of 10% until it reaches zero, resulting in 396×398 grid points with a constant coarser mesh in the interior of the domain. The time-step used in the simulations is 0.01. An extensive mesh and time-step dependency analysis has been carried out to ensure that the solutions are grid-free and accurate.

3.3. Benchmark

As stated in Section 2.5, it is expected that accurate DNS results from the scaled equations, in the region $y \gg y_{c,s}$, should match the exact solution (58) and (59). Fig. 5 contains the DNS results and the exact solution of the horizontal profiles of the vertical velocity and temperature at $Re = 1$ (with $s = 10$ and $Pr = 0.1$), 10 (with $s = 1$ and $Pr = 0.1$) and 100 (with $s = 1$ and $Pr = 0.01$) respectively in the upper, y independent, region of the flow. A quantitative comparison between numerical and exact solutions for temperature θ at the specific location $x = 0.01$ and maximum vertical velocity v_m within the boundary layer at

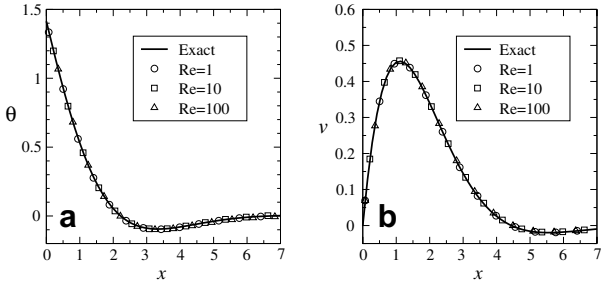

Fig. 5. Numerical vertical velocity and temperature profiles at $Re = 1$ (with $s = 10$ and $Pr = 0.1$), 10 (with $s = 1$ and $Pr = 0.1$) and 100 (with $s = 1$ and $Pr = 0.01$), respectively, compared to the exact solution.

Table 1
A comparison between numerical and exact solutions for temperature θ at the specific location $x = 0.01$ and maximum vertical velocity v_m within the boundary layer at $Re = 1$ (with $s = 10$ and $Pr = 0.1$), 10 (with $s = 1$ and $Pr = 0.1$) and 100 (with $s = 1$ and $Pr = 0.01$), respectively

		$Re = 1$ ($s = 10$, $Pr = 0.1$)	$Re = 10$ ($s = 1$, $Pr = 0.1$)	$Re = 100$ ($s = 1$, $Pr = 0.01$)
$\theta_{x=0.01}$	Exact	1.400072	1.400072	1.400072
	Numerical	1.400029	1.401752	1.402032
	Error	−0.0031%	0.12%	0.14%
v_m	Exact	0.455842	0.455842	0.455842
	Numerical	0.455806	0.457459	0.457560
	Error	−0.008%	0.35%	0.38%

these three Re's is also presented in Table 1, which, together with Fig. 5, clearly shows that the numerical solutions match the analytic solution, indicating that the DNS results are accurate.

4. DNS results

In this section, the scaling laws obtained above are validated and quantified by a series of DNS with selected values of Pr and s in the ranges of $0.01 \leqslant Pr \leqslant 0.5$ and $0.2 \leqslant s \leqslant 5$ with the resulting Reynolds number in the range of $1 \leqslant Re \leqslant 100$. The numerically quantified steady-state scaling laws will also be tested against the exact solution. A total of 10 DNS runs have been carried out for this purpose, it ie, Runs 1–6 with $Pr = 0.01$, 0.025, 0.05, 0.075, 0.1 and 0.5 while keeping $s = 1$ unchanged have been carried out to examine the Pr dependence of the scaling laws, whereas Runs 7–10 and 5 with $s = 0.2$, 0.5, 2, 5, and 1 while keeping $Pr = 0.1$ unchanged are for the examination of the s dependence.

It should be noted that the wall temperature θ_w and the thermal boundary-layer thickness δ_T have essentially the same scaling relations with Pr and s at various stages of the boundary-layer development, as shown above. In fact, the DNS results show that the only differences between the quantified scaling laws for θ_w and those for δ_T are their respective values of the proportionality constants in the scaling laws. To avoid repetition, only the DNS results for θ_w are therefore presented here.

4.1. Scaling laws for θ_w scales

The scaling laws for θ_w, $\theta_{w,e}$, and $\theta_{w,s}$ are Eqs. (38), (44), and (49), as obtained above, where θ_w, $\theta_{w,e}$, and $\theta_{w,s}$ are dimensionless wall temperatures during the start-up stage (when $\tau < \tau_{w,e}$), at the end of the start-up stage (when $\tau = \tau_{w,e}$), and at steady state (when $\tau > \tau_s$) respectively. The scaling laws for $\tau_{w,e}$ and $\tau_{w,p}$ are Eqs. (41) and (51), where $\tau_{w,e}$ and $\tau_{w,p}$ are respectively the dimensionless time for the development of the wall temperature to come to the end of the start-up stage and the dimensionless half-period of the oscillation presented in the time series of θ_w at the transitional stage.

Fig. 6 presents the DNS results of θ_w plotted against $s^{1/2}\tau^{1/2}$ with the variations of y, Pr, and s during the start-up stage and at the transitional stage and steady state. Figs. 6a and b contain the DNS results with the y variation for the specific case of $Pr = 0.1$ and $s = 1$ (Run 5). The results show that the scaled time series at $y = 30$, 50, 70, and 90, which are much larger than $y_{c,e}$ and $y_{c,s}$ (1.96 and 1 respectively for this specific case), overlay each other, clearly demonstrating that the development of θ_w at all stages is independent of y and is one-dimensional when $y \gg y_{c,e}$ and $y \gg y_{c,s}$, which is in agreement with the scaling law (38). The slight deviation of the scaled $y = 10$ series is because the conditions $y \gg y_{c,e}$ and $y \gg y_{c,s}$ are not well met. This y-independence is also true for the whole velocity boundary-layer thickness δ_v, the inner velocity boundary-layer thickness δ_{vi}, and the maximum velocity v_m, as will be shown below. Fig. 6a also show that the scaling $\tau^{1/2}$ brings all five series onto a single straight line described by

$$\theta_w = 1.085 s^{1/2}\tau^{1/2}, \tag{67}$$

at the early start-up stage (when $\tau < \tau_{w,e}$ and τ is not close to $\tau_{w,e}$), validating that $\tau^{1/2}$ is the correct scaling in Eq. (38) at this portion of the start-up stage. When τ approaches $\tau_{w,e}$ (i.e., at the later portion of the start-up stage), it is observed that the scaled series, although still overlaying each other, gradually deviate from the quantified scaling law (67). This

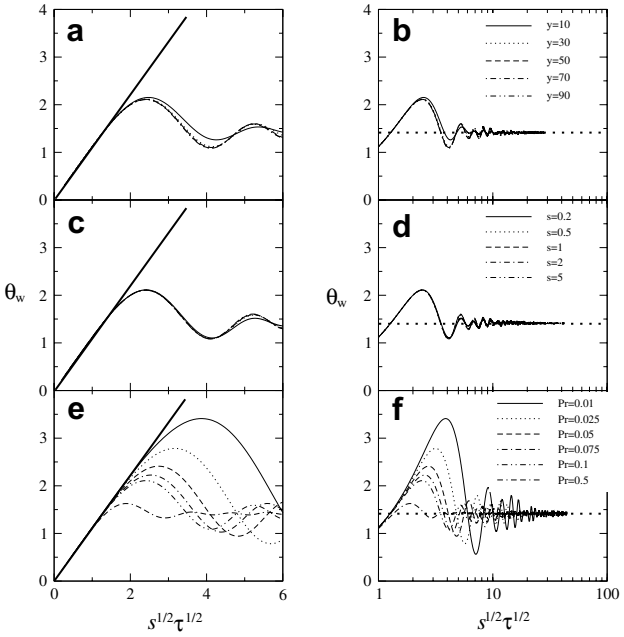

Fig. 6. DNS results of θ_w plotted against $s^{1/2}\tau^{1/2}$ at the start-up stage (left column) and at the transitional stage and steady state (right column): (a) and (b) for the y variation with $Pr = 0.1$ and $s = 1$; (c) and (d) for the s variation with $Pr = 0.1$ at $y = 90$; and (e) and (f) for the Pr variation with $s = 1$ at $y = 90$. — (bold, left column), $\theta_w = 1.085 s^{1/2}\tau^{1/2}$; and ⋯ (bold, right column), $\theta_{w,s} = 1.414$.

deviation is the result of the shifting of the dominant balance in Eq. (4) from the initial unsteady-conduction balance to the convection–conduction balance, as noted in the scaling analysis. At the end of the start-up stage (when $\tau = \tau_{w,e}$), all values of $\theta_{w,e}$ at different y have approximately the same value of 2.110 and the scaled time series come to the end of the start-up stage almost at the same time, with $\tau_{w,e} = 5.784$, showing that $\tau_{w,e}$ is also independent of y which is in line with the scaling law (41). At steady state (when $\tau > \tau_s$, according to Eq. (47), $\tau_s \sim 1/(sPr) \sim 10$ in this specific case), all values of $\theta_{w,s}$ at different y approach 1.414, which is in fact the exact solution given by Eq. (60), clearly showing that the DNS results are not only in agreement with the scaling law (49), but also validated by the exact solution.

Fig. 6c contains the DNS results with the s variation at $y = 90$ when $Pr = 0.1$ (Runs 5, 7–10) during the start-up stage, showing that the $s^{1/2}$ scaling brings all five time series onto the same single straight line described by Eq. (67) at the early start-up stage, which confirms that $s^{1/2}$ is the correct scaling in the scaling law (38). At the end of the start-up stage, all five scaled time series essentially reach the same maximum value of 2.110, showing that $\theta_{w,e}$ is independent of s, which agrees with the scaling law (44). Fig. 6d contains the DNS results with the s variation at $y = 90$ when $Pr = 0.1$ at the transitional stage and the steady state, showing that all five series with different s approach the exact solution of $\theta_{w,s} = 1.414$ at steady state, again confirming the scaling law (49).

Fig. 6e contains the DNS results with the Pr variation at $y = 90$ when $s = 1$ (Runs 1–6) during the start-up stage, showing that all six scaled time series with different Pr fall onto the same single straight line described by Eq. (67) at the early start-up stage. However, they reach the ends of their individual start-up stages at quite different times and their values of $\theta_{w,e}$ are also considerably different, showing that $\theta_{w,e}$ and $\tau_{w,e}$ are Pr dependent, as predicted by the scaling laws (44) and (41). Fig. 6f contains the DNS results with the Pr variation at $y = 90$ when $s = 1$ at the transitional stage and the steady state, showing that all six series with different Pr approach the exact solution of $\theta_{w,s} = 1.414$ at steady state, confirming once more the scaling law (49).

The Pr dependence of $\theta_{w,e}$ and $\tau_{w,e}$, as predicted by the scaling laws (44) and (41), are $\theta_{w,e} \sim Pr^{-1/4}(1 - Pr^{1/2})^{-1/4}$ and $\tau_{w,e} \sim Pr^{-1/2}(1 - Pr^{1/2})^{-1/2}$ respectively, which, along with other scaling laws, are validated by the DNS results as presented in Fig. 7. Fig. 7a shows that all values of $\theta_{w,e}$, with the variations of y, s and Pr, fall onto a single straight line described by

$$\theta_{w,e} = \frac{1.051}{Pr^{1/4}(1 - Pr^{1/2})^{1/4}}, \tag{68}$$

which confirms the scaling law (44). Similarly, Fig. 7b shows that all values of $\tau_{w,e}$ with the variations of y, s and Pr fall onto a single straight line described by

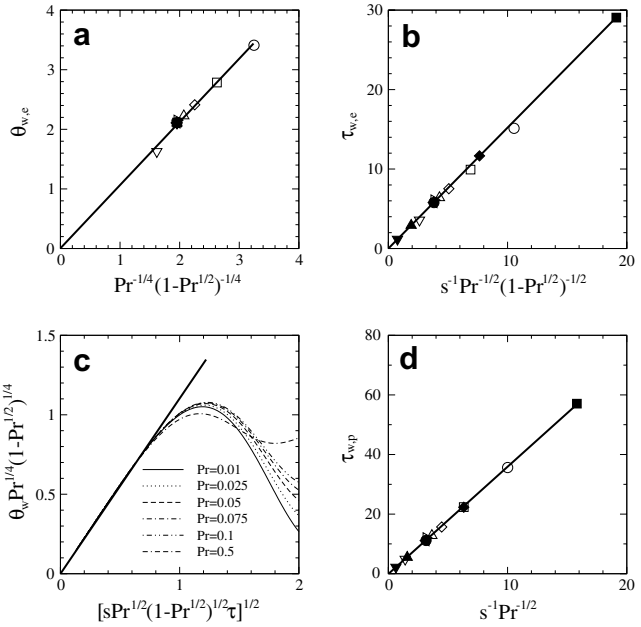

Fig. 7. DNS results for (a) $\theta_{w,e}$ plotted against $Pr^{-1/4}(1 - Pr^{1/2})^{-1/4}$; (b) $\tau_{w,e}$ plotted against $s^{-1}Pr^{-1/2}(1 - Pr^{1/2})^{-1/2}$; (c) $\theta_w Pr^{1/4}(1 - Pr^{1/2})^{1/4}$ plotted against $[sPr^{1/2}(1 - Pr^{1/2})^{1/2}\tau]^{1/2}$; and (d) $\tau_{w,p}$ plotted against $s^{-1}Pr^{-1/2}$. Symbols used in (a), (b) and (d): ○, $Pr = 0.01$, $s = 1$ and $y = 90$; □, $Pr = 0.025$, $s = 1$ and $y = 90$; ◇, $Pr = 0.05$, $s = 1$ and $y = 90$; △, $Pr = 0.075$, $s = 1$ and $y = 90$; ◁, $Pr = 0.1$, $s = 1$ and $y = 90$; ▽, $Pr = 0.5$, $s = 1$ and $y = 90$; ▷, $Pr = 0.1$, $s = 1$ and $y = 10$; +, $Pr = 0.1$, $s = 1$ and $y = 30$; ×, $Pr = 0.1$, $s = 1$ and $y = 50$; ●, $Pr = 0.1$, $s = 1$ and $y = 70$; ■, $Pr = 0.1$, $s = 0.2$ and $y = 90$; ♦, $Pr = 0.1$, $s = 0.5$ and $y = 90$; ▲, $Pr = 0.1$, $s = 2$ and $y = 90$; ▼, $Pr = 0.1$, $s = 5$ and $y = 90$.

$$\tau_{w,e} = \frac{1.518}{sPr^{1/2}(1 - Pr^{1/2})^{1/2}}, \tag{69}$$

which confirms the scaling law (41). The same time series with the Pr variation presented in Fig. 6e are re-plotted in Fig. 7c, but θ_w and τ are now scaled by $Pr^{-1/4}(1 - Pr^{1/2})^{-1/4}$ and $s^{-1}Pr^{-1/2}(1 - Pr^{1/2})^{-1/2}$ which are the scales for $\theta_{w,e}$ and $\tau_{w,e}$ respectively, as predicted by the scaling laws (44) and (41). The scaled series are now observed to attain approximately the same peak at almost the same time, with slight deviations for the extreme values of Pr considered, i.e., $Pr = 0.01$ and 0.5, and again all scaled series with different Pr fall onto the same single straight line described by Eq. (67) at the early start-up stage, once again confirming the scaling laws (44) and (41). Fig. 7d shows that all values of $\tau_{w,p}$ with the variations of y, s and Pr fall onto a single straight line described by

$$\tau_{w,p} = \frac{3.569}{sPr^{1/2}}, \tag{70}$$

which confirms the scaling law (51).

4.2. Scaling laws for δ_v scales

As noted above, the scaling laws (38), (44), (49), (41) and (51) are also valid for δ_v, $\delta_{v,w,e}$, $\delta_{v,s}$, $\tau_{v,e}$ and $\tau_{v,p}$ respectively, where δ_v, $\delta_{v,w,e}$, and $\delta_{v,s}$ are the dimensionless whole velocity

boundary-layer thickness during the start-up stage of θ_w (when $\tau < \tau_{w,e}$), at the end of the start-up stage of θ_w (when $\tau = \tau_{w,e}$), and at steady state of δ_v itself (when $\tau > \tau_s$) respectively, whereas $\tau_{v,e}$ and $\tau_{v,p}$ are the dimensionless time for the development of δ_v to come to the end of its start-up stage and the dimensionless half-period of the oscillation presented in the time series of δ_v at the transitional stage.

Fig. 8 presents the DNS results of δ_v plotted against $s^{1/2}\tau^{1/2}$ with the variations of y, Pr, and s during the start-up stage and at the transitional stage and steady state. Figs. 8a and b contain the DNS results with the y variation for the specific case of $Pr = 0.1$ and $s = 1$ (Run 5). Similar to θ_w, it is observed that all series except that at $y = 10$ overlay each other, confirming that the development of δ_v at all stages is also independent of y and is one-dimensional when $y \gg y_{c,e}$ and $y \gg y_{c,s}$. It is further found that all five scaled series fall onto a single straight line described by

$$\delta_v = 2.134 s^{1/2}\tau^{1/2}, \tag{71}$$

at the early start-up stage (when $\tau < \tau_{v,e}$ and τ is not very close to $\tau_{v,e}$), validating that $\tau^{1/2}$ is the correct scaling in Eq. (38) at this portion of the start-up stage. When τ approaches $\tau_{v,e}$ (that is at the later portion of the start-up stage), it is observed that the scaled time series, excepting the $y = 10$ series, although still overlaying each other, gradually deviate from the quantified scaling law (71) due to the shifting of the dominant balance in Eq. (4) as noted above for θ_w. At the end of the start-up stage (when $\tau = \tau_{v,e}$), all values of $\delta_{v,e}$ except that at $y = 10$ have approximately

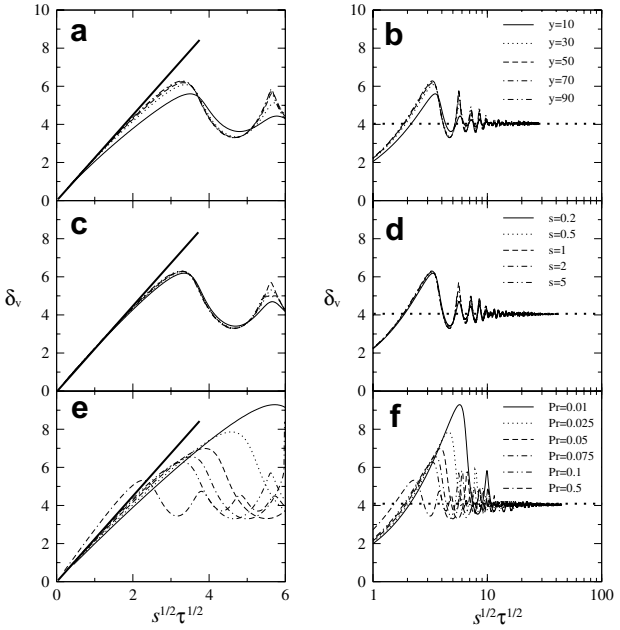

Fig. 8. DNS results of δ_v plotted against $s^{1/2}\tau^{1/2}$ at the start-up stage (left column) and at the transitional stage and steady state (right column): (a) and (b) for the y variation with $Pr = 0.1$ and $s = 1$; (c) and (d) for the s variation with $Pr = 0.1$ at $y = 90$; and (e) and (f) for the Pr variation with $s = 1$ at $y = 90$. — (bold, left column), $\delta_v = 2.134 s^{1/2}\tau^{1/2}$; and ··· (bold, right column), $\delta_{v,s} = 4.040$.

the same value of 6.279 and the scaled time series come to the end of the start-up stage at almost the same time, with $\tau_{v,e} = 10.856$, confirming that $\tau_{v,e}$ is also independent of y which is in line with the scaling law (41). At steady state (when $\tau > \tau_s$), all values of $\delta_{v,s}$ at different y approach 4.040, which is the exact solution given by Eq. (66), clearly showing that the DNS results are not only in agreement with the scaling law (49), but also validated by the exact solution.

Fig. 8c contains the DNS results with the s variation at $y = 90$ when $Pr = 0.1$ (Runs 5, 7–10) during the start-up stage, showing that the $s^{1/2}$ scaling brings all five series onto the same straight line described by (71) at the early start-up stage, confirming that $s^{1/2}$ is the correct scaling in (38) for δ_v. At the end of the start-up stage, all five scaled series essentially reach the same maximum value of 6.279, validating that $\delta_{v,e}$ is independent of s. Fig. 8d contains the DNS results with the s variation at $y = 90$ when $Pr = 0.1$ at the transitional stage and the steady state, showing that all five series with different s approach the exact solution of $\delta_{v,s} = 4.040$ at steady state, again confirming the scaling law (49).

Fig. 8e contains the DNS results with the Pr variation at $y = 90$ when $s = 1$ (Runs 1–6) during the start-up stage. Although it is observed that the scaling $\tau^{1/2}$ brings all six time series onto straight lines at the early start-up stage, these lines do not overlay each other and the series reach the ends of their individual start-up stages at quite different times and have considerably varying values of $\delta_{v,e}$, showing that $\delta_{v,e}$ and $\tau_{v,e}$ are Pr dependent. The Pr dependence of $\tau_{v,e}$ is predicted by the scaling law (41). Although it is expected that δ_v at $\tau = \tau_{w,e}$, i.e., $\delta_{v,w,e}$, is predicted by the scaling law (44), it does not mean that this law will apply for $\delta_{v,e}$ when it reaches the end of its own start-up stage at $\tau = \tau_{v,e}$, as $\tau_{v,e}$ is usually much larger than $\tau_{w,e}$ (for example, when $Pr = 0.1$ and $s = 1$, $\tau_{w,e}$ at $y = 90$ is 5.784, but $\tau_{v,e}$ is 10.856). On the other hand, the scaling law (49) predicts that $\delta_{v,s} \sim 1$ at steady state (when $\tau > \tau_s$), which is confirmed by the DNS results presented in Fig. 8f for $y = 90$ and $s = 1$, where it is shown that all six series with different Pr approach the exact solution of $\delta_{v,s} = 4.040$ at steady state.

As noted above, when the development of δ_v proceeds from the end of the start-up stage of θ_w (i.e., $\delta_{v,w,e}$) to steady state (i.e., $\delta_{v,s}$), the corresponding scaling law for δ_v will change from (44), i.e., $\delta_{v,w,e} \sim Pr^{-1/4}(1 - Pr^{1/2})^{-1/4}$ at $\tau = \tau_{w,e}$ to (49), i.e., $\delta_{v,s} \sim 1$ at steady state ($\tau > \tau_s$). It is therefore expected that a combination of these two scalings shall provide a correct prediction for $\delta_{v,e}$ at $\tau = \tau_{v,e}$ if $\tau_{w,e} < \tau_{v,e} < \tau_s$, i.e., the scaling law for $\delta_{v,e}$ is expected to be as follows:

$$\delta_{v,e} \sim \frac{1}{Pr^{1/4}(1 - Pr^{1/2})^{1/4}} + 1. \tag{72}$$

To verify the scaling law (72), the DNS results of $\delta_{v,e}$ are plotted against $[1 + Pr^{-1/4}(1 - Pr^{1/2})^{-1/4}]$ in Fig. 9a for

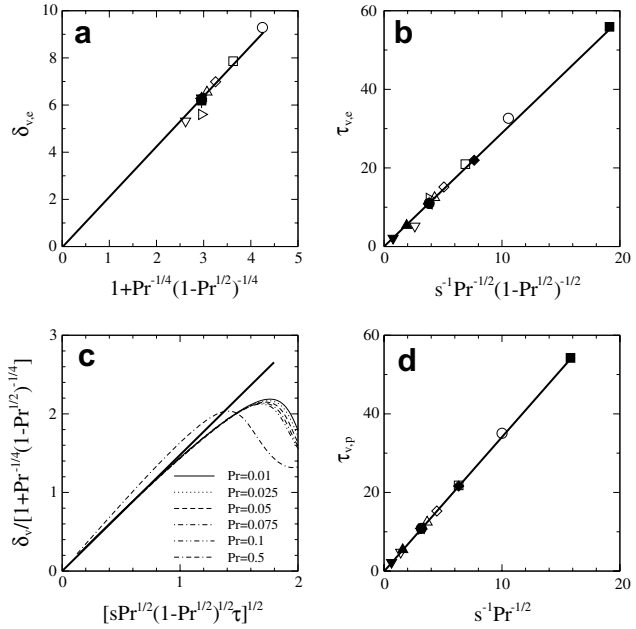

Fig. 9. DNS results for (a) $\delta_{v,e}$ plotted against $[1+Pr^{-1/4}(1-Pr^{1/2})^{-1/4}]$; (b) $\tau_{v,e}$ plotted against $s^{-1}Pr^{-1/2}(1-Pr^{1/2})^{-1/2}$; (c) $\delta_v/[1+Pr^{-1/4}(1-Pr^{1/2})^{-1/4}]$ plotted against $[sPr^{1/2}(1-Pr^{1/2})^{1/2}\tau]^{1/2}$; and (d) $\tau_{v,p}$ plotted against $s^{-1}Pr^{-1/2}$. For the symbols used in (a), (b) and (d) see the caption of Fig. 7.

the variations of y, Pr, and s, which shows that all values of $\delta_{v,e}$ fall onto a single straight line described by

$$\delta_{v,e}=\frac{2.127}{1+Pr^{-1/4}(1-Pr^{1/2})^{-1/4}}, \tag{73}$$

confirming the scaling law (72).

The DNS results of $\tau_{v,e}$ are plotted against $s^{-1}Pr^{-1/2}(1-Pr^{1/2})^{-1/2}$ in Fig. 9b for the variations of y, Pr, and s, which shows that all values of $\tau_{v,e}$ fall onto a single straight line described by

$$\tau_{v,e}=\frac{2.889}{sPr^{1/2}(1-Pr^{1/2})^{1/2}}, \tag{74}$$

confirming the scaling law (41).

The same time series with the Pr variation presented in Fig. 8e are re-plotted in Fig. 9c, but here δ_v and τ are scaled by $[1+Pr^{-1/4}(1-Pr^{1/2})^{-1/4}]$ and $s^{-1}Pr^{-1/2}(1-Pr^{1/2})^{-1/2}$ which are the scales for $\delta_{v,e}$ and $\tau_{v,e}$ respectively. All series except $Pr=0.5$ are observed to attain approximately the same scaled peak at almost the same scaled time and fall onto the same straight line described by

$$\frac{\delta_v}{1+Pr^{-1/4}(1-Pr^{1/2})^{-1/4}}=1.478\left[sPr^{1/2}(1-Pr^{1/2})^{1/2}\tau\right]^{1/2}, \tag{75}$$

at the early start-up stage, further confirming the scaling laws (72) and (41). However, it is also observed that the scaled series with $Pr=0.5$ has a large deviation from the quantified scaling. It should be noted that the scaling law (72) is only valid for $\tau_{w,e}<\tau_{v,e}<\tau_s$, as noted above, which, with (41) and (47), requires

$$\frac{1}{sPr^{1/2}(1-Pr^{1/2})^{1/2}}<\frac{1}{sPr}, \tag{76}$$

i.e., $Pr<[(\sqrt{5}-1)/2]^2$ which gives $Pr<0.382$, and therefore the quantified scaling law (75) obtained above is only valid for $Pr<0.382$ and the observed large deviation for the $Pr=0.5$ series is therefore not a surprise as it does not meet the requirement of $Pr<0.382$.

The DNS results of $\tau_{v,p}$ are plotted against $s^{-1}Pr^{-1/2}$ in Fig. 9d for the variations of y, Pr, and s, which shows that all values of $\tau_{v,p}$ fall onto a single straight line described by

$$\tau_{v,p}=\frac{3.413}{sPr^{1/2}}, \tag{77}$$

confirming that (51) is the correct scaling law for $\tau_{v,p}$.

4.3. Scaling laws for v_m scales

The scaling laws for v_m, $v_{m,w,e}$, $v_{m,s}$, $\tau_{m,e}$ and $\tau_{m,p}$ are Eqs. (40), (43), (50), (41) and (51) respectively, as obtained in the scaling analysis, where v_m, $v_{m,w,e}$, and $v_{m,s}$ are dimensionless maximum vertical velocity in the boundary layer during the start-up stage of θ_w (when $\tau<\tau_{w,e}$), at the end of the start-up stage of θ_w (when $\tau=\tau_{w,e}$), and at steady state of v_m itself (when $\tau>\tau_s$) respectively, whereas $\tau_{m,e}$ and $\tau_{m,p}$ are the dimensionless time for the development of v_m to come to the end of its start-up stage and the dimensionless half-period of the oscillation presented in the time series of v_m at the transitional stage.

Fig. 10 presents the DNS results of v_m plotted against $s^{3/2}Pr(1-Pr^{1/2})\tau^{3/2}$ with the variations of y, Pr, and s during the start-up stage and at the transitional stage and steady state. Figs. 10a and b contain the DNS results with the y variation for the specific case of $Pr=0.1$ and $s=1$ (Run 5), showing that the development of v_m at all stages is also independent of y and is one-dimensional when $y\gg y_{c,e}$ and $y\gg y_{c,s}$, the same as that for θ_w and δ_v. It is also found that all five scaled series fall onto a single straight line described by

$$v_m=0.488s^{3/2}Pr(1-Pr^{1/2})\tau^{3/2}, \tag{78}$$

at the early start-up state (when $\tau<\tau_{w,e}$ and τ is far away from $\tau_{m,e}$), validating that $\tau^{3/2}$ is the correct scaling in Eq. (40) at this portion of the start-up stage. Beyond $\tau_{w,e}$, it is observed that the scaled series, although still overlaying each other with the exception of the $y=10$ series, gradually deviate from the quantified scaling law (78) due to the shifting of the dominant balance in Eq. (4) as noted above for θ_w. At the end of the start-up stage (when $\tau=\tau_{m,e}$), all values of $v_{m,e}$ except that at $y=10$ have approximately the same value of 0.606 and the scaled series come to the end of the start-up stage almost at the same time, with $\tau_{m,e}=10.935$, confirming that $\tau_{m,e}$ is also independent of y which agrees with the scaling law (41). At steady state (when $\tau>\tau_s$), all values of $v_{m,s}$ at different y approach

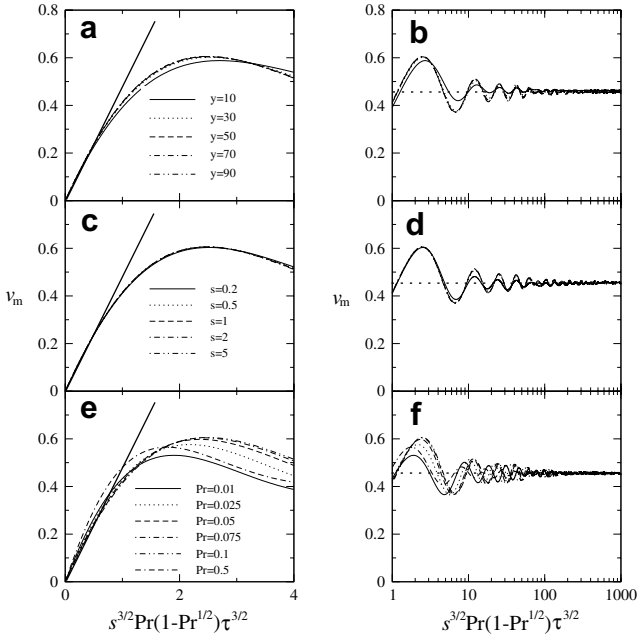

Fig. 10. DNS results of v_m plotted against $s^{3/2}Pr(1-Pr^{1/2})\tau^{3/2}$ at the start-up stage (left column) and at the transitional stage and steady state (right column): (a) and (b) for the y variation with $Pr = 0.1$ and $s = 1$; (c) and (d) for the s variation with $Pr = 0.1$ at $y = 90$; and (e) and (f) for the Pr variation with $s = 1$ at $y = 90$. — (bold, left column), $v_m = 0.488s^{3/2}Pr(1-Pr^{1/2})\tau^{3/2}$; and $\cdots$ (bold, right column), $v_{m,s} = 0.455$.

0.455, which is the exact solution given by Eq. (62), clearly showing that the DNS results are not only in agreement with the scaling law (50), but also validated by the exact solution.

Fig. 10c contains the DNS results with the s variation at $y = 90$ when $Pr = 0.1$ (Runs 5, 7–10) during the start-up stage, showing that the $s^{3/2}$ scaling brings all five series to fall onto the same straight line described by Eq. (78) at the early start-up stage, confirming that $s^{3/2}$ is the correct scaling in (40) for v_m at this portion of the start-up stage. At the end of the start-up stage, all five scaled series essentially reach the same maximum value of 0.606, validating that $v_{m,e}$ is independent of s. Fig. 10d contains the DNS results with the s variation at $y = 90$ when $Pr = 0.1$ at the transitional stage and the steady state, showing that all five series with different s approach the exact solution of $v_{m,s} = 0.455$ at steady state, again confirming the scaling law (50).

Fig. 10e contains the DNS results with the Pr variation at $y = 90$ when $s = 1$ (Runs 1–6) during the start-up stage, showing that at the early start-up stage (when τ is much smaller than $\tau_{m,e}$) the scaling $Pr(1-Pr^{1/2})$ brings all series to fall approximately onto the same line described by Eq. (78), although slight deviations are observed for the extreme values of Pr considered, i.e., for $Pr = 0.01$ and 0.5, which clearly demonstrates that $Pr(1-Pr^{1/2})$ is the correct scaling for v_m at the early start-up stage. The DNS results also show that the series with different values of Pr reach the ends of their individual start-up stages at quite different times (i.e., at different values of $\tau_{m,e}$) and have considerably varied values of $v_{m,e}$ as well, showing that $v_{m,e}$ and $\tau_{m,e}$ are Pr dependent. The Pr dependence of $\tau_{m,e}$ is again predicted by the scaling law (41), the same as that for $\tau_{v,e}$. Although it is expected that v_m at $\tau = \tau_{w,e}$, i.e., $v_{m,w,e}$, is predicted by the scaling law (43), however, similar to $\delta_{v,e}$, it does not mean that it will apply for $v_{m,e}$ when it reaches the end of its own start-up stage at $\tau = \tau_{m,e}$, as $\tau_{m,e}$, like $\tau_{v,e}$, is also usually much larger than $\tau_{w,e}$ (in fact, as will be shown below, the DNS results demonstrate that $\tau_{m,e}$ is essentially equal to $\tau_{v,e}$ for all values of s and Pr considered. For example, for $Pr = 0.1$, $s = 1$ and $y = 90$, $\tau_{m,e} = 10.935$ and $\tau_{v,e} = 10.856$. Both are much larger than $\tau_{w,e}$ which is 5.784). On the other hand, the scaling law (50) predicts that $v_{m,s} \sim 1$ at steady state (when $\tau > \tau_s$), which is confirmed by the DNS results presented in Fig. 10f for $y = 90$ and $s = 1$, where it is shown that all six series with different Pr approach the exact solution of $v_{m,s} = 0.455$ at steady state.

As described in the scaling analysis, when the development of v_m proceeds from the end of the start-up stage of θ_w (i.e., $v_{m,w,e}$) to steady state (i.e., $v_{m,s}$), the corresponding scaling law for v_m will change from (43), i.e., $v_{m,w,e} \sim Pr^{1/4}(1-Pr^{1/2})^{1/4}$ at $\tau = \tau_{w,e}$ to (50), i.e., $v_{m,s} \sim 1$ at steady state ($\tau > \tau_s$). It is therefore expected that, similar to $\delta_{v,e}$, a combination of these two scalings shall provide a correct prediction for $v_{m,e}$ at $\tau = \tau_{m,e}$ if $\tau_{w,e} < \tau_{m,e} < \tau_s$, i.e., the scaling law for $v_{m,e}$ is expected to be as follows:

$$v_{m,e} \sim 1 + Pr^{1/4}(1-Pr^{1/2})^{1/4}. \tag{79}$$

To verify the scaling law (79), the DNS results of $v_{m,e}$ are plotted against $[1 + Pr^{1/4}(1-Pr^{1/2})^{1/4}]$ in Fig. 11a for the variations of y, Pr, and s, which shows that all values of $v_{m,e}$ fall onto a single straight line described by

$$v_{m,e} = \frac{0.408}{1 + Pr^{1/4}(1-Pr^{1/2})^{1/4}}, \tag{80}$$

confirming the scaling law (79).

The DNS results of $\tau_{m,e}$ are plotted against $s^{-1}Pr^{-1/2}(1-Pr^{1/2})^{-1/2}$ in Fig. 11b for the variations of y, Pr, and s, which shows that all values of $\tau_{m,e}$ fall onto a single straight line described by

$$\tau_{m,e} = \frac{2.889}{sPr^{1/2}(1-Pr^{1/2})^{1/2}}, \tag{81}$$

which is in fact the quantified scaling law obtained above for $\tau_{v,e}$, confirming the scaling law (41) as well as demonstrating that $\tau_{m,e}$ is essentially equal to $\tau_{v,e}$ for all values of s and Pr considered, as noted above.

The same time series with the Pr variation presented in Fig. 10e are re-plotted in Fig. 11c, but here v_m and τ are scaled by $[1 + Pr^{1/4}(1-Pr^{1/2})^{1/4}]$ and $s^{-1}Pr^{-1/2}(1-Pr^{1/2})^{-1/2}$ which are scales for $v_{m,e}$ and $\tau_{m,e}$ respectively. All series except the $Pr = 0.5$ one are observed to attain approximately the same scaled peak at almost the same scaled time and fall onto the same straight line described by

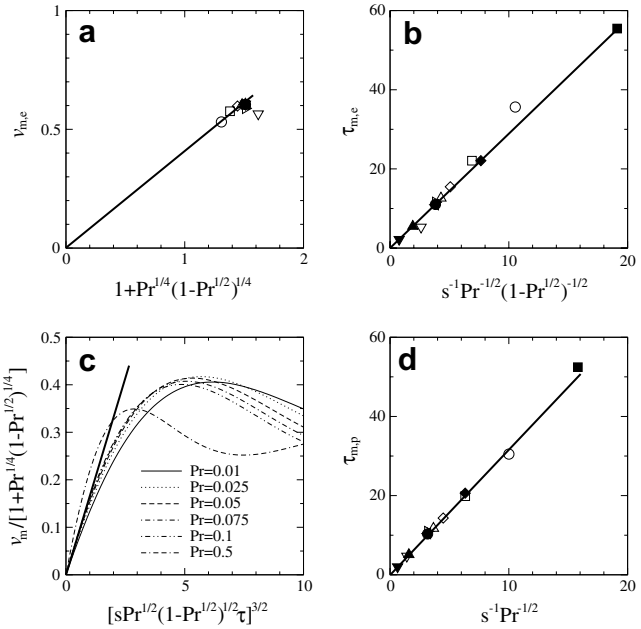

Fig. 11. DNS results for (a) $v_{m,e}$ plotted against $[1+Pr^{1/4}(1-Pr^{1/2})^{1/4}]$; (b) $\tau_{m,e}$ plotted against $s^{-1}Pr^{-1/2}(1-Pr^{1/2})^{-1/2}$; (c) $v_m/[1+Pr^{1/4}\times(1-Pr^{1/2})^{1/4}]$ plotted against $[sPr^{1/2}(1-Pr^{1/2})^{1/2}\tau]^{3/2}$; and (d) $\tau_{m,p}$ plotted against $s^{-1}Pr^{-1/2}$. For the symbols used in (a), (b) and (d) see the caption of Fig. 7.

$$\frac{v_m}{1+Pr^{1/4}(1-Pr^{1/2})^{1/4}} = 0.166\left[sPr^{1/2}(1-Pr^{1/2})^{1/2}\tau\right]^{1/2}. \tag{82}$$

at the early start-up stage, further confirming the scaling laws (79) and (41). The large deviation of the $Pr = 0.5$ series from this quantified scaling law is due to the same reason as explained for δ_v, i.e., the quantified scaling law (82) obtained above is valid for $Pr < 0.382$ only. The large deviation of the $Pr = 0.5$ data from the quantified scaling law $v_{m,e} = 0.408/[1+Pr^{1/4}(1-Pr^{1/2})^{1/4}]$, as shown in Fig. 11a, is due to the same reason.

The DNS results of $\tau_{m,p}$ are plotted against $s^{-1}Pr^{-1/2}$ in Fig. 11d for the variations of y, Pr, and s, which shows that all values of $\tau_{m,p}$ fall onto a single straight line described by

$$\tau_{m,p} = \frac{3.160}{sPr^{1/2}}, \tag{83}$$

confirming that (51) is the correct scaling law for $\tau_{m,p}$.

4.4. Scaling laws for δ_{vi} scales

The scaling laws for δ_{vi}, $\delta_{vi,w,e}$, $\delta_{vi,s}$, $\tau_{vi,e}$ and $\tau_{vi,p}$ are Eqs. (39), (45), (49), (41) and (51) respectively, as obtained in the scaling analysis, where δ_{vi}, $\delta_{vi,w,e}$, and $\delta_{vi,s}$ are dimensionless inner velocity boundary-layer thickness during the start-up stage of θ_w (when $\tau < \tau_{w,e}$), at the end of the start-up stage of θ_w (when $\tau = \tau_{w,e}$), and at steady state of δ_{vi} itself (when $\tau > \tau_s$) respectively, whereas $\tau_{vi,e}$ and $\tau_{vi,p}$ are the dimensionless time for the development of δ_{vi} to come to the end of its start-up stage and the dimensionless half-period of the oscillation presented in the time series of δ_{vi} at the transitional stage.

Fig. 12 presents the DNS results of δ_{vi} plotted against $s^{1/2}Pr^{1/2}\tau^{1/2}$ with the variations of y, Pr, and s during the start-up stage and at the transitional stage and steady state. Figs. 12a and b contain the DNS results with the y variation for the specific case of $Pr = 0.1$ and $s = 1$ (Run 5), showing that the development of δ_{vi} at all stages is also independent of y and is one-dimensional when $y \gg y_{c,e}$ and $y \gg y_{c,s}$, same as that for θ_w, δ_v and v_m. It is also found that all five scaled series fall onto a single straight line described by

$$\delta_{vi} = 1.238s^{1/2}Pr^{1/2}\tau^{1/2}, \tag{84}$$

at the early start-up state (when $\tau < \tau_{w,e}$ and τ is far away from $\tau_{vi,e}$), validating that $\tau^{1/2}$ is the correct scaling in Eq. (39) at this portion of the start-up stage. Beyond $\tau_{w,e}$, it is observed that the scaled series, although still overlaying each other with the exception of the $y = 10$ series, gradually deviate from the quantified scaling law (84) due to the shifting of the dominant balance as noted above. At the end of the start-up stage (when $\tau = \tau_{vi,e}$), all values of $\delta_{vi,e}$ except that at $y = 10$ have approximately the same value of 1.208 and the scaled series come to the end of the start-up stage almost at the same time, with $\tau_{vi,e} = 14.104$, confirming that $\tau_{vi,e}$ is also independent of y which agrees with the scaling law (41). At steady state (when $\tau > \tau_s$), all

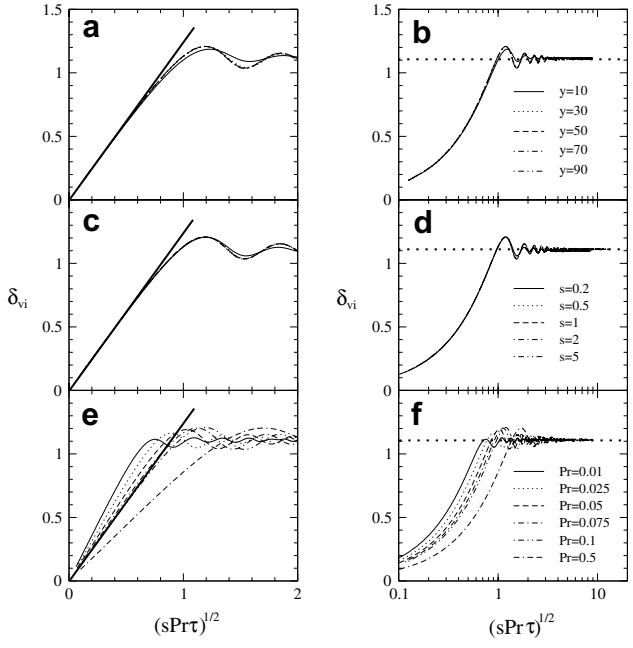

Fig. 12. DNS results of δ_{vi} plotted against $s^{1/2}Pr^{1/2}\tau^{1/2}$ at the start-up stage (left column) and at the transitional stage and steady state (right column): (a) and (b) for the y variation with $Pr = 0.1$ and $s = 1$; (c) and (d) for the s variation with $Pr = 0.1$ at $y = 90$; and (e) and (f) for the Pr variation with $s = 1$ at $y = 90$. — (bold, left column), $\delta_{vi} = 1.238s^{1/2}Pr^{1/2}\tau^{1/2}$; and ··· (bold, right column), $\delta_{vi,s} = 1.111$.

values of $\delta_{vi,s}$ at different y approach 1.111, which is the exact solution given by Eq. (63), clearly showing that the DNS results are not only in agreement with the scaling law (49), but also validated by the exact solution.

Fig. 12c contains the DNS results with the s variation at $y = 90$ when $Pr = 0.1$ (Runs 5, 7–10) during the start-up stage, showing that the $s^{1/2}$ scaling brings all five series to fall onto the same straight line described by Eq. (84) at the early start-up stage, confirming that $s^{1/2}$ is the correct scaling in (39) for δ_{vi} at this portion of the start-up stage. At the end of the start-up stage, all five scaled series essentially reach the same maximum value of 1.208, validating that $\delta_{vi,e}$ is independent of s. Fig. 12d contains the DNS results with the s variation at $y = 90$ when $Pr = 0.1$ at the transitional stage and the steady state, showing that all five series with different s approach the exact solution of $\delta_{vi,s} = 1.111$ at steady state, again confirming the scaling law (49).

Fig. 12e contains the DNS results with the Pr variation at $y = 90$ when $s = 1$ (Runs 1–6) during the start-up stage, showing that at the early start-up stage (when τ is much smaller than $\tau_{vi,e}$) the scaling $Pr^{1/2}$ brings all series to fall onto straight lines, however, these lines do not overlay each other and the series reach the ends of their individual start-up stages at quite different times and have considerably varied values of $\delta_{vi,e}$, showing that $\delta_{vi,e}$ and $\tau_{vi,e}$ are Pr dependent. The Pr dependence of $\tau_{vi,e}$ is again predicted by the scaling laws (41). Similar to $\delta_{v,e}$ and $v_{m,e}$, although it is expected that δ_{vi} at $\tau = \tau_{w,e}$, i.e., $\delta_{vi,w,e}$, is predicted by the scaling law (45), however, it does not mean that it will apply for $\delta_{vi,e}$ when it reaches the end of its own start-up stage at $\tau = \tau_{vi,e}$, as $\tau_{vi,e}$ is usually much larger than $\tau_{w,e}$ (for example, when $Pr = 0.1$ and $s = 1$, $\tau_{w,e}$ at $y = 90$ is 5.784, but $\tau_{vi,e}$ is 14.104). On the other hand, the scaling law (49) predicts that $\delta_{vi,s} \sim 1$ at steady state (when $\tau > \tau_s$), which is confirmed by the DNS results presented in Fig. 12f for $y = 90$ and $s = 1$, where it is shown that all series with different Pr approach the exact solution of $\delta_{vi,s} = 1.111$ at steady state.

Similar to δ_{vo} and v_m, when the development of δ_{vi} proceeds from the end of the start-up stage of θ_w (i.e., $\delta_{vi,w,e}$) to steady state (i.e., $\delta_{vi,s}$), the corresponding scaling law for δ_{vi} will change from (45), i.e., $\delta_{vi,w,e} \sim Pr^{1/4}(1 - Pr^{1/2})^{-1/4}$ at $\tau = \tau_{vi,e}$ to (49), i.e., $\delta_{vi,s} \sim 1$ at steady state ($\tau > \tau_s$). It is therefore expected that a combination of these two scalings will provide a correct prediction for $\delta_{vi,e}$ at $\tau = \tau_{vi,e}$ if $\tau_{w,e} < \tau_{vi,e} < \tau_s$, i.e., the scaling law for $\delta_{vi,e}$ is expected to be as follows:

$$\delta_{vi,e} \sim 1 + \frac{Pr^{1/4}}{(1 - Pr^{1/2})^{1/4}}. \tag{85}$$

To verify the scaling law (85), the DNS results for $\delta_{vi,e}$ are plotted against $[1 + Pr^{1/4}(1 - Pr^{1/2})^{-1/4}]$ in Fig. 13a for the variations of y, Pr, and s, which shows that all values of $\delta_{vi,e}$ fall approximately onto a single straight line described by

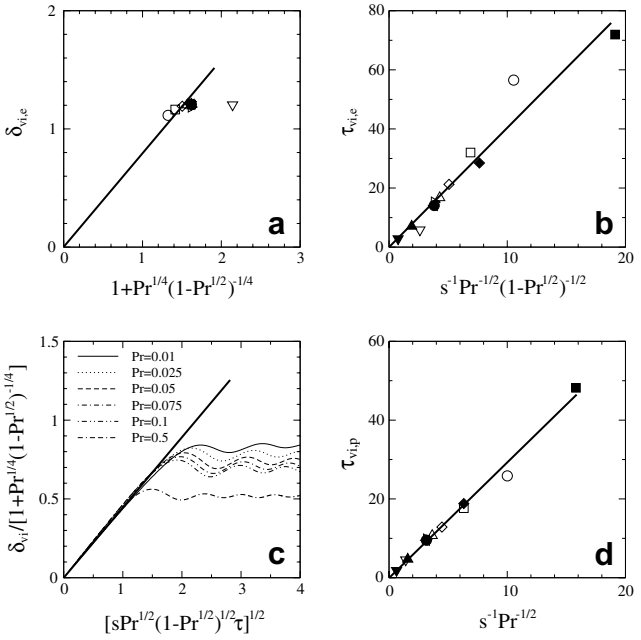

Fig. 13. DNS results for (a) $\delta_{vi,e}$ plotted against $[1 + Pr^{1/4}(1 - Pr^{1/2})^{-1/4}]$; (b) $\tau_{vi,e}$ plotted against $s^{-1}Pr^{-1/2}(1 - Pr^{1/2})^{-1/2}$; (c) $\delta_{vi}/[1 + Pr^{1/4}(1 - Pr^{1/2})^{-1/4}]$ plotted against $[sPr^{1/2}(1 - Pr^{1/2})^{1/2}\tau]^{1/2}$; and (d) $\tau_{vi,p}$ plotted against $s^{-1}Pr^{-1/2}$. For the symbols used in (a), (b) and (d) see the caption of Fig. 7.

$$\delta_{vi,e} = \frac{0.793}{1 + Pr^{1/4}(1 - Pr^{1/2})^{-1/4}}, \tag{86}$$

confirming the scaling law (85).

The DNS results for $\tau_{vi,e}$ are plotted against $s^{-1}Pr^{-1/2}(1 - Pr^{1/2})^{-1/2}$ in Fig. 13b for the variations of y, Pr, and s, which shows that all values of $\tau_{vi,e}$ fall onto a single straight line described by

$$\tau_{m,e} = \frac{4.038}{sPr^{1/2}(1 - Pr^{1/2})^{1/2}}, \tag{87}$$

confirming the scaling law (41).

The same time series with the Pr variation presented in Fig. 12e are re-plotted in Fig. 13c, but here δ_{vi} and τ are scaled by $[1 + Pr^{1/4}(1 - Pr^{1/2})^{-1/4}]$ and $s^{-1}Pr^{-1/2}(1 - Pr^{1/2})^{-1/2}$ which are the scales for $\delta_{vi,e}$ and $\tau_{vi,e}$ respectively, showing that these scales bring all series with different Pr to fall onto a single straight line described by

$$\frac{\delta_{vi}}{1 + Pr^{1/4}(1 - Pr^{1/2})^{-1/4}} = 0.446\left[sPr^{1/2}(1 - Pr^{1/2})^{1/2}\tau\right]^{1/2}. \tag{88}$$

at the early start-up stage, further confirming the scaling laws (85) and (41). The reason for the large deviation of the $Pr = 0.5$ series is the same as that noted above for δ_v and v_m, i.e., the quantified scaling law (88) obtained above is also valid for $Pr < 0.382$ only. The large deviation of the $Pr = 0.5$ data from the quantified scaling law (86), as shown in Fig. 13a, is due to the same reason.

The DNS results of $\tau_{m,p}$ are plotted against $s^{-1}Pr^{-1/2}$ in Fig. 13d for the variations of y, Pr, and s, which shows that all values of $\tau_{m,p}$ fall onto a single straight line described by

$$\tau_{m,p} = \frac{3.160}{sPr^{1/2}}, \tag{89}$$

confirming that (51) is the correct scaling law for $\tau_{m,p}$.

5. Conclusions

A set of scaling laws have been derived to describe the basic features of unsteady natural convection boundary-layer flow of an initially linearly-stratified fluid adjacent to an evenly heated semi-infinite vertical plate with isoflux boundary condition. The scaling laws have been developed for fluids with $Pr < 1$ with the intention, in particular, of determining the Pr effect for such flows, especially before the flow attains the steady state. The scaling laws obtained for the steady-state one-dimensional flow have been benchmarked by the exact solution showing that they match the exact solution. All the scaling laws have also been validated by a series of direct numerical simulations which provide a full description of the flow behavior.

The dominant parameters characterizing the flow behavior are the plate temperature, maximum vertical velocity, thermal boundary-layer thickness, whole and inner velocity boundary-layer thicknesses, and the corresponding times at various development stages. For stratified fluids like the one considered here, oscillations will be present at the transitional stage, and their features are also of interest and were investigated in this work. The scaling analysis shows that the development of the boundary layer is independent of y under the conditions that $y \gg y_{c,e}$ during the start-up stage and $y \gg y_{c,s}$ at steady state, otherwise it is y-dependent.

The velocity boundary layer consists of an inner and an outer region that require separate scalings. In the inner region the behavior of the velocity before attaining steady state is determined by an unsteady-viscous balance in the vertical momentum equation. In the outer region, however, the velocity boundary layer is governed by an unsteady–buoyancy balance, as has been verified.

The DNS results have verified the dependences of the basic flow features on Pr and s and have also determined the values of the various constants of proportionality presented in the scaling laws obtained from the scaling analysis.

Acknowledgements

The authors wish to acknowledge the support of the Australian Research Council. W. Lin also wish to acknowledge the support from the National Natural Science Foundation of China (10262003), the Natural Science Foundation of Yunnan Province of China (Key Project 2003E0004Z), the Program for New Century Excellent Talents in University (NCET-04-0918), and the JCU Faculty Grant Scheme.

References

[1] Y. Jaluria, Natural Convection Heat and Mass Transfer, Pergamon, Oxford, 1980.
[2] B. Gebhart, Y. Jaluria, R.L. Mahajan, B. Sammakia, Buoyancy-Induced Flows and Transport, Hemisphere, New York, 1988.
[3] J.M. Hyun, Unsteady bouyant convection in an enclosure, Adv. Heat Transfer 24 (1994) 277–320.
[4] A. Bejan, Convection Heat Transfer, second ed., John Wiley & Sons, New York, 1995.
[5] R.J. Goldstein, E.R.G. Eckert, W.E. Ibele, et al., Heat transfer – a review of 2002 literature, Int. J. Heat Mass Transfer 48 (2005) 819–927.
[6] M.J. Stewart, F. Weinberg, Fluid flow in liquid metals, I. Theoretical analysis, J. Crystal Growth 12 (1972) 217–227.
[7] A.A. Mohamad, R. Viskanta, Transient natural convection of low-Prandtl-number fluids in a differentially heated cavity, Int. J. Numer. Methods Fluids 13 (1991) 61–81.
[8] H. Sammouda, A. Belghith, C. Surry, Finite element simulation of transient natural convection of low-Prandtl-number fluids in heated cavity, Int. J. Numer. Methods Heat Fluid Flow 9 (1999) 612–624.
[9] E.M. Sparrow, J.L. Gregg, Laminar free convection from a vertical plate with uniform surface heat flux, Trans. ASME 78 (1956) 435–440.
[10] H.K. Kuiken, Free convection at low Prandtl numbers, J. Fluid Mech. 37 (1969) 785–798.
[11] E.R.G. Eckert, Introduction to the Transfer of Heat and Mass, McGraw-Hill, New York, 1950.
[12] R.L. Mahajan, B. Gebhart, Higher order approximations to the natural convection flow over a uniform flux vertical surface, Int. J. Heat Mass Transfer 21 (1978) 549–556.
[13] K.H. Park, V.P. Carey, Analysis of transient natural convection flow near a vertical surface at low Prandtl number, Numer. Heat Transfer 8 (1985) 317–333.
[14] J.H. Merkin, A note on the similarity solutions for free convection on a vertical plate, J. Eng. Math. 19 (1985) 189–201.
[15] J.H. Merkin, Free convection on a heated vertical plate: the solution for small Prandtl number, J. Eng. Math. 23 (1989) 273–282.
[16] J.H. Merkin, I. Pop, T. Mahmood, Mixed convection on a vertical surface with a prescribed heat flux: the solution for small and large Prandtl numbers, J. Eng. Math. 25 (1991) 165–190.
[17] G. Ramanaiah, G. Malarvizhi, Unified treatment of free convection adjacent to a vertical plate with three thermal boundary conditions, Wärme Stoffübertrag. 27 (1992) 393–396.
[18] I. Di Piazza, M. Ciofalo, Low-Prandtl number natural convection in volumetrically heated rectangular enclosure I. Slender cavity, $AR = 4$, Int. J. Heat Mass Transfer 43 (2000) 3027–3051.
[19] S. Arcidiacono, I. Di Piazza, M. Ciofalo, Low-Prandtl number natural convection in volumetrically heated rectangular enclosure II. Square cavity. $AR = 1$, Int. J. Heat Mass Transfer 44 (2001) 537–550.
[20] S. Arcidiacono, M. Ciofalo, Low-Prandtl number natural convection in volumetrically heated rectangular enclosure II. Shallow cavity, $AR = 0.25$, Int. J. Heat Mass Transfer 44 (2001) 3053–3065.
[21] J.S. Park, J.M. Hyun, Transient behavior of vertical buoyancy layer in a stratified fluid, Int. J. Heat Mass Transfer 41 (1998) 4393–4397.
[22] J.S. Park, J.M. Hyun, Transient motion of a confined stratified fluid induced simultaneously by sidewall thermal loading and vertical throughflow, J. Fluid Mech. 451 (2002) 295–317.
[23] A.J. Chamkha, Laminar hydromagnetic natural convection flow along a heated vertical surface in a stratified environment with internal heat absorption, Can. J. Phys. 80 (2002) 1145–1156.
[24] A. Shaprio, E. Fedorovich, Unsteady convectively driven flow along a vertical plate immersed in a stably stratified fluid, J. Fluid Mech. 498 (2004) 333–352.

[25] A. Shaprio, E. Fedorovich, Prandtl number dependence of unsteady natural convection along a vertical plate in a stably stratified fluid, Int. J. Heat Mass Transfer 47 (2004) 4911–4927.
[26] L. Prandtl, Essentials of Fluid Dynamics, Blackie, London, 1952, pp. 422–425.
[27] J.C. Patterson, J. Imberger, Unsteady natural convection in a rectangular cavity, J. Fluid Mech. 100 (1980) 65–86.
[28] W. Lin, S.W. Armfield, Direct simulation of natural convection cooling in a vertical circular cylinder, Int. J. Heat Mass Transfer 42 (1999) 4117–4130.
[29] W. Lin, S.W. Armfield, Natural convection cooling of rectangular and cylindrical containers, Int. J. Heat Fluid Flow 22 (2001) 72–81.
[30] W. Lin, S.W. Armfield, Long-term behavior of cooling fluid in a rectangular container, Phys. Rev. E 69 (2004) 056315.
[31] W. Lin, S.W. Armfield, Long-term behavior of cooling fluid in a vertical cylinder, Int. J. Heat Mass Transfer 48 (2005) 53–66.
[32] W. Lin, S.W. Armfield, P.L. Morgan, Unsteady natural convection boundary-layer flow along a vertical isothermal plate in a linearly stratified fluid, Int. J. Heat Mass Transfer 45 (2002) 451–459.
[33] J.S. Turner, Buoyancy Effects in Fluids, Cambridge University Press, Cambridge, 1973.
[34] W. Lin, S.W. Armfield, Unsteady natural convection on an evenly heated vertical plate for Prandtl number $Pr < 1$, Phys. Rev. E 72 (2005) 066309.
[35] S.W. Armfield, Finite difference solutions of the Navier–Stokes equations on staggered and non-staggered grids, Comput. Fluids 20 (1991) 1–17.
[36] S.W. Armfield, J.C. Patterson, Wave properties of natural-convection boundary layers, J. Fluid Mech. 239 (1992) 195–211.
[37] W. Lin, S.W. Armfield, Direct simulation of weak axisymmetric fountains in a homogeneous fluid, J. Fluid Mech. 403 (2000) 67–88.
[38] W. Lin, S.W. Armfield, Weak fountains in a stratified fluid, Phys. Rev. E 66 (2002) 066308.